Magnetic Field Resilience of Three-Dimensional Transmons with Thin-Film Al/AlO$_x$/Al Josephson Junctions Approaching 1 T

J. Krause,[1,‡] C. Dickel,[1,†,‡] E. Vaal,[1,2] M. Vielmetter,[1] J. Feng,[1] R. Bounds,[1] G. Catelani,[2] J. M. Fink,[3] and Yoichi Ando[1,*]

[1] *Physics Institute II, University of Cologne, Zülpicher Str. 77, Köln 50937, Germany*
[2] *JARA Institute for Quantum Information (PGI-11), Forschungszentrum Jülich, Jülich 52425, Germany*
[3] *Institute of Science and Technology Austria, Klosterneuburg 3400, Austria*

(Received 29 October 2021; revised 20 December 2021; accepted 4 January 2022; published 11 March 2022)

Magnetic-field-resilient superconducting circuits enable sensing applications and hybrid quantum computing architectures involving spin or topological qubits and electromechanical elements, as well as studying flux noise and quasiparticle loss. We investigate the effect of in-plane magnetic fields up to 1 T on the spectrum and coherence times of thin-film three-dimensional aluminum transmons. Using a copper cavity, unaffected by strong magnetic fields, we can probe solely the effect of magnetic fields on the transmons. We present data on a single-junction and a superconducting-quantum-interference-device (SQUID) transmon that are cooled down in the same cavity. As expected, the transmon frequencies decrease with increasing field, due to suppression of the superconducting gap and a geometric Fraunhofer-like contribution. Nevertheless, the thin-film transmons show strong magnetic field resilience: both transmons display microsecond coherence up to at least 0.65 T, and T_1 remains above 1 μs over the entire measurable range. SQUID spectroscopy is feasible up to 1 T, the limit of our magnet. We conclude that thin-film aluminum Josephson junctions are suitable hardware for superconducting circuits in the high-magnetic-field regime.

DOI: 10.1103/PhysRevApplied.17.034032

I. INTRODUCTION

Josephson junctions (JJs) based on aluminum and its oxide (Al/AlO$_x$/Al) have three key properties that have made them the workhorse of circuit QED (cQED) [1]. They are routinely fabricated to high quality; their Josephson energy E_J can be estimated from the room-temperature resistance [2]; and E_J can be controlled with high yield to specifications [3] using standard electron beam lithography, and even tuned postfabrication [4,5]. These properties have enabled various advances in quantum engineering, for example the scaling up of quantum processors to more than 50 qubits [6] and the fabrication of sophisticated Josephson parametric amplifiers [7]. The cQED framework allows one to elucidate the quantum mechanical interactions of various systems with photons, enabling us to understand those systems from a new perspective. As standard JJ circuits continue to advance, cQED is also being applied to more exotic systems such as nonconventional JJs, mechanical elements, magnons, quantum dots, spin qubits, and Majorana zero modes [8].

When cQED methods are to be applied to phenomena or systems requiring strong magnetic fields, the magnetic field compatibility of the components used in cQED becomes an issue. So far, this issue has been explored as the need arose. One component that is particularly useful is the superconducting quantum interference device (SQUID): two JJs in parallel form a SQUID. SQUIDs are an important tool in, e.g., metrology [9], and a key building block in many cQED quantum computing architectures [10–12]. Compatibility of a SQUID with high magnetic fields enables, e.g., the study of spin ensembles or even single spins. In this context, SQUIDs based on constriction junctions have demonstrated operation up to 6 T [13]. There is currently a lot of interest in using SQUIDs in external magnetic fields to couple mechanical oscillators to superconducting circuits [14–20]. Magnetic fields are also a requirement for integrating many spin-qubit architectures with cQED [21,22], and for many Majorana-zero-mode realizations [23,24], where cQED methods could be used for readout [25]. To couple to quantum dots and topological qubits, magnetic-field-resilient superconducting resonators have been realized [26–28]. But the exploration of superconducting qubits in magnetic fields has so far largely relied on semiconductor nanowire JJs [29–31], graphene JJs [32], or JJs based on granular aluminum [33], with

*ando@ph2.uni-koeln.de
†dickel@ph2.uni-koeln.de
‡These authors contributed equally to this work.

qubits based on carbon-nanotube JJs likely to follow soon [15,34]. A notable exception was presented in Ref. [35], which explored a standard single-junction $Al/AlO_x/Al$ transmon in a magnetic field, but the findings suggest that coherence times are already severely limited at an in-plane field of 20 mT. So far, qubit designs based on non-standard JJs have reached higher magnetic fields, but have not consistently achieved the reliability, quality, and targeting of E_J that $Al/AlO_x/Al$-JJ qubits routinely achieve.

In this paper, we explore the magnetic field dependence of the Josephson energy E_J and the coherence of transmon qubits [36] with standard $Al/AlO_x/Al$ JJs in a three-dimensional (3D) copper cavity [37,38]. The 3D copper cavity is essentially unaffected by the magnetic field and thus allows us to explore the magnetic field dependence of the transmons without additional complications. Planar superconducting resonators are themselves vulnerable to magnetic fields, which proved to be a limiting factor in Ref. [35]. We first show the spectrum as a function of the out-of-plane magnetic field and demonstrate how the limitations imposed on qubit coherence by vortices require precise alignment. With the use of a vector magnet, we can align the magnetic field axis with the sample plane to high precision. Thus, we can measure the transmon spectrum and coherence as a function of the exact in-plane magnetic field. We track the transition frequencies of the transmons over a range of approximately 1–7 GHz in in-plane magnetic fields of up to 1 T. Based on the spectrum, we try to understand the geometric effects and the magnetic field dependence of the superconducting gap. One of the transmons has a SQUID loop; therefore, we can investigate combining very sensitive SQUIDs with large magnetic fields. Overall, even the SQUID transmon maintains sufficient coherence for many of the applications mentioned above. Thus, we show that $Al/AlO_x/Al$ JJs can be operated in high magnetic fields to give coherent qubits matching the demonstrated field compatibility of nonstandard superconductor–normal-metal–superconductor JJs [31].

II. EXPERIMENTAL SETUP

In Fig. 1, we display the 3D copper cavity containing the two transmons, the transmon geometries, and a sketch relating the JJ geometry to the magnetic field axes. The cavity design is based on Ref. [39]. There is one asymmetric SQUID transmon and one single-JJ transmon; each has its own merits. On the one hand, the SQUID transmon is sensitive to microtesla out-of-plane fields $B_\perp$, allowing precise alignment of the magnetic field parallel to the device plane. It is also tunable, meaning measurements can cover a wide frequency range, allowing us to estimate frequency effects in a similar magnetic field. On the other hand, the single-JJ transmon is less sensitive to flux noise and to magnetic field misalignment, and thus it serves as a control device for the SQUID transmon. As

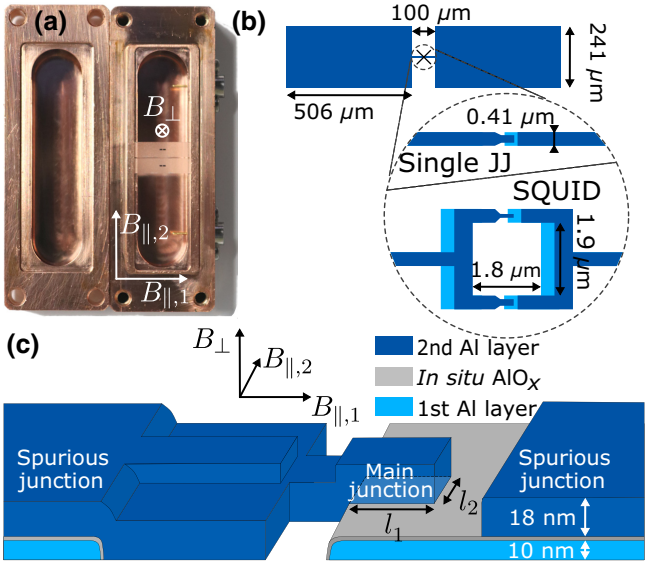

FIG. 1. (a) 3D copper cavity with two transmons, referred to as the single-Josephson-junction transmon and the SQUID transmon. (b) Top view of the transmons, with enlargement of the junction region for both the single-JJ and the SQUID device. (c) Sketch of a Dolan-bridge JJ, relating the magnetic field coordinate system ($B_{\parallel,1}$,$B_{\parallel,2}$,$B_\perp$) to the JJ geometry.

shown in Fig. 1(b), the 3D transmons have long narrow leads to the JJ, making them vortex resilient, even though the large capacitor pads do not have intentional vortex-trapping sites. Having no magnetic shields, we opted for a small SQUID loop area of 3.4 μm^2.

The JJs are made to a standard Dolan-bridge design [40] with double-shadow evaporation, but for field compatibility we choose a thickness of only 10 nm for the first aluminum layer and 18 nm for the second layer. The JJs presented are made in the same fabrication run; scanning electron micrographs of the junction region can be found in Appendix A. The design leads to large spurious JJs [see Fig. 1(c)] between the two superconducting films, which could complicate the in-plane magnetic field dependence [35]. For more detailed information on the device and on the experimental setup, see Ref. [41].

III. OUT-OF-PLANE MAGNETIC FIELD DEPENDENCE

For every in-plane magnetic field for which results are shown in this paper, we sweep the out-of-plane magnetic field, $B_\perp$. In contrast to Ref. [42], where vortex-quasiparticle interplay is explored, we do not perform field cooling; rather, we change the magnetic field with the sample remaining at the base temperature, as in Ref. [43]. The out-of-plane-field data sets for different in-plane fields are qualitatively similar, even at the highest fields at which all quantities can be measured. As an example,

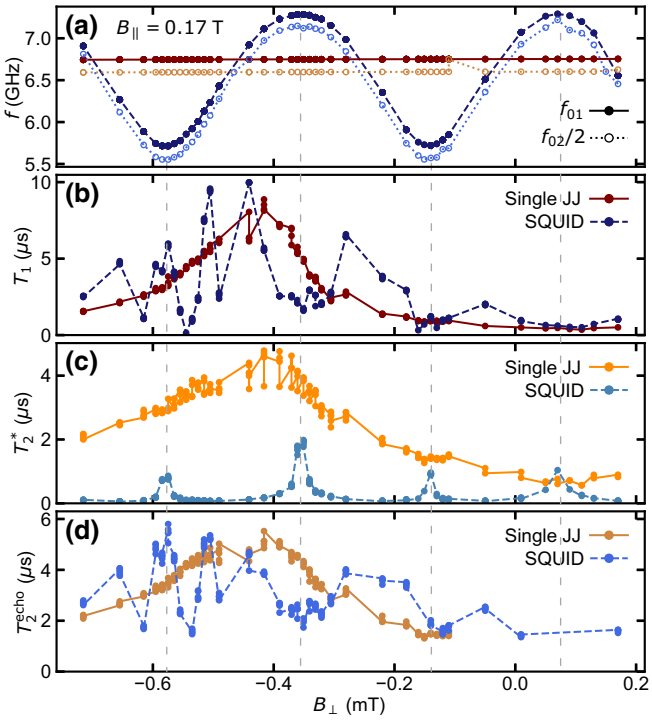

FIG. 2. Out-of-plane magnetic field dependences of the two transmons, shown here for $B_{\parallel,1} = 0.17$ T. (a) First and second transmon transitions f_{01} and $f_{02}/2$. The SQUID transmon changes with the out-of-plane magnetic field $B_\perp$ that threads the SQUID loop. As its constituent JJs are asymmetric, the frequencies oscillate between top and bottom limits, the sweet spots. (b) Energy relaxation time T_1. High T_1 is found in a $B_\perp$ interval from -0.7 mT to -0.25 mT, deviating from the nominal $B_\perp = 0$ based on the SQUID alignment procedure. (c) Ramsey dephasing time T_2^*. At the sweet spots, the SQUID frequency is less sensitive to flux noise, and T_2^* is enhanced. (d) Echo dephasing time $T_2^{\rm echo}$. In the interval of high T_1, $T_2^{\rm echo}$ is generally not limited by $2T_1$ for either transmon.

Fig. 2(a) shows two-tone spectroscopy peaks of the transmon frequencies for a $B_\perp$ range of approximately 1 mT at $B_{\parallel,1} = 0.17$ T (a data set for $B_{\parallel,1} = 0$ T can be found in Ref. [41]). We always measure both the first and the second excitation energies of the transmons, f_{01} and $f_{02}/2$, to be able to estimate E_J and the charging energy E_C. [29,35]. While the frequency of the single-JJ transmon changes by only approximately 10 MHz over this range in $B_\perp$, the SQUID-transmon frequency oscillates between top and bottom limits, the sweet spots. The sweet spots are determined by the sum and difference of the E_J's of the constituent JJs. Models for the $B_\perp$ dependence of the spectrum for both transmons can be found in Appendix E.

We also measure the relaxation time T_1 and the Ramsey and Hahn-echo dephasing times T_2^* and $T_2^{\rm echo}$ of the transmons for different values of $B_\perp$ at a fixed $B_{\parallel,1}$. One can see in Figs. 2(b)–2(d) that both transmons show higher coherence at a finite $B_\perp$ (around $B_\perp \simeq 0.4$ mT). The $B_\perp = 0$ point is based on aligning the parallel magnetic field based on the SQUID oscillations (Appendix B). Therefore we have to sweep $B_\perp$ at every value of the in-plane magnetic field and map out the value at which T_1 is maximized; we call this B_0 and consider it to be an offset in the perpendicular-field dependence. The offset B_0 seems to follow a roughly linear trend as a function of $B_{\parallel,1}$. This is an interesting observation, likely related to vortex physics, but we do not have a concrete understanding at this point (for more details, see Appendix C).

Apart from the existence of B_0, to understand the effect of $B_\perp$ on T_1, we consider loss due to superconducting vortices coupling to the transmon current (see Appendix D for details) and the Purcell limit imposed by the cavity (see Appendix G). For the single-JJ transmon, the frequency remains practically constant when $B_\perp$ is swept, and thus the change in T_1 is likely to be due to vortices. The loss scales linearly with $B_\perp - B_0$ sufficiently far away from the maximum T_1, but the onset of vortex loss is not linear. For the SQUID transmon, we consistently find T_1 to be lower at the top sweet spot than at the bottom sweet spot. Looking at the frequency dependence of T_1, we find that for high frequencies it is Purcell limited (see Appendix G). The B_0 values for a given $B_{\parallel,1}$ are similar for both transmons (see also Appendix B).

The dephasing times for both transmons do not reach $2T_1$ in the high-T_1 interval. Close to the cavity resonance frequency, photon shot noise from the cavity is a limiting factor on $T_2^{\rm echo}$ (see Appendix G). Compared with the single-JJ transmon, the SQUID transmon shows a drastically reduced T_2^*, with a clear sweet-spot enhancement. For $T_2^{\rm echo}$, the sweet-spot enhancement is less clear. Thus, the SQUID-transmon data point to slow noise in $B_\perp$, limiting T_2^* but not $T_2^{\rm echo}$.

IV. IN-PLANE MAGNETIC FIELD DEPENDENCE OF THE SPECTRUM

Next we consider the in-plane magnetic field dependences of the two transmons. Here we focus on the data obtained for the $B_{\parallel,1}$ direction. For every value of the in-plane-field $B_{\parallel,1}$, we sweep $B_\perp$ to perform a full set of measurements, as explained in Sec. III. First, we show how the transmon spectra evolve in a parallel magnetic field. As one can see in Fig. 3(b), both transmons decrease in frequency at higher magnetic fields. As the magnetic field increases, the difference between the SQUID's top and bottom sweet-spot frequencies [Fig. 3(a)], indicating that the E_J's of the two constituent JJs evolve differently. For high $B_{\parallel,1}$, we observe large charge-parity splitting due to the decreasing E_J/E_C ratio. Thus, the two parity branches of f_{01} are plotted for $B_{\parallel,1} = 0.88$ T.

Having measured f_{01} and $f_{02}/2$ for both transmons, we can estimate E_J (and E_C) as described in Appendix E. For the high-field low-E_J/E_C-ratio regions, charge-parity

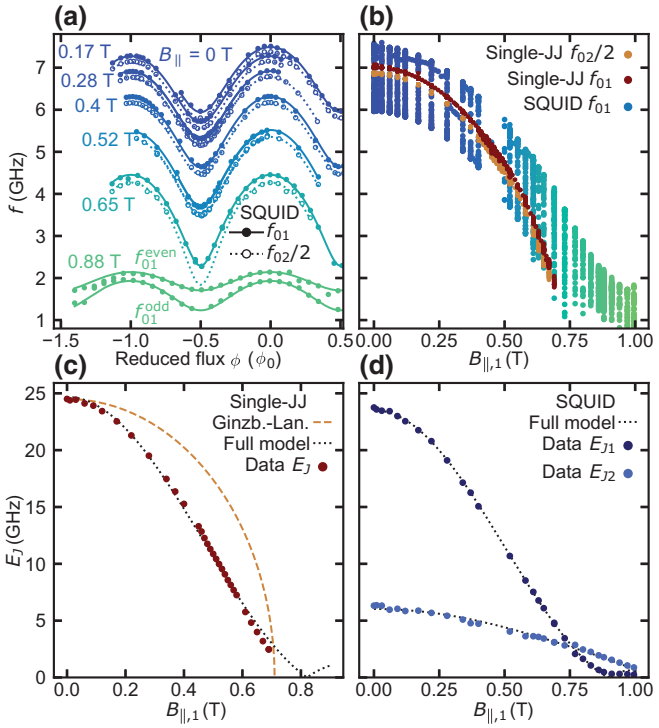

FIG. 3. Spectroscopy for in-plane magnetic fields. (a) Examples of the flux dependence of the SQUID transmon frequency: for every $B_{\parallel,1}$, we sweep $B_\perp$ to tune the SQUID transmon. We measure f_{01} and $f_{02}/2$. With increasing $B_{\parallel,1}$ [the color scale corresponds to that in (b)], both frequencies decrease, and eventually the $f_{02}/2$ transition can no longer be measured. For high $B_{\parallel,1}$, f_{01} is split into curves for even and odd charge parity, shown for $B_{\parallel,1} = 0.88$ T. (b) Transitions f_{01} for SQUID transmon and f_{01},$f_{02}/2$ for single-JJ transmon versus in-plane magnetic field $B_{\parallel,1}$. (c) Extracted Josephson energy E_J for the single-JJ transmon. We correct for several different systematic errors; for details, see Appendix E. A simple Ginzburg-Landau theory for the superconducting gap provides neither qualitative nor quantitative agreement. By combining the GL theory with the flux penetration into an extended junction, Eq. (1), we obtain better agreement (dotted line). (d) Josephson energies E_J for the two Josephson junctions forming the asymmetric SQUID transmon. The E_{J1} of the larger junction is consistent with a second Fraunhofer lobe emerging for $B_{\parallel,1} > 0.9$ T.

splitting is used to estimate E_J. The resulting E_J as a function of $B_{\parallel,1}$ is shown in Figs. 3(c) and 3(d) for the single-JJ and the SQUID transmon, respectively. A naive estimate based on the Ginzburg-Landau (GL) theory for the superconducting gap provides neither qualitative nor quantitative agreement for the in-plane field dependence of E_J [Fig. 3(c)]. We therefore combine the GL theory with a Fraunhofer term describing the flux penetration into an extended junction,

$$E_J(B_\parallel) = E_{J0}\sqrt{1-\left(\frac{B_\parallel}{B_\parallel^{\mathrm{crit}}}\right)^2}\left|\mathrm{sinc}\left(\frac{B_\parallel}{B_{\Phi_0}}\right)\right|, \quad (1)$$

TABLE I. Parameters of the three JJs. To determine B_{Φ_0}, the in-plane field at which a superconducting flux quantum threads the JJ, we fit Eq. (1) to the data in Figs. 3(c) and 3(d), assuming the same GL critical field $B_\parallel^{\mathrm{crit}} = 1.03$ T for all JJs. Then B_{Φ_0} should be inversely proportional to the junction finger width l_2, as determined by SEM imaging.

	$E_J(B_{\parallel,1}=0)$	B_{Φ_0}	l_2
Single JJ	24.7 GHz	0.83 T	231 nm
SQUID JJ_1	23.5 GHz	0.90 T	206 nm
SQUID JJ_2	6 GHz	1.65 T	122 nm

where E_{J0} denotes the Josephson energy at zero field, $B_\parallel^{\mathrm{crit}}$ the in-plane Ginzburg-Landau critical field, and B_{Φ_0} the in-plane field at which one superconducting flux quantum ($= h/2e$) threads the JJ. B_{Φ_0} is inversely proportional to the in-plane cross section of the junction, defined by its finger width l_2 [see Fig. 1(c)] and the constant insulator thickness. As the JJs differ in finger width, each JJ has a different B_{Φ_0}. Assuming the same critical field $B_\parallel^{\mathrm{crit}} = 1.03$ T for all three junctions, we find that the independently measured junction dimensions are consistent with the estimated B_{Φ_0} (Table I). Taking the values for l_2 and B_{Φ_0}, we can calculate the height of the in-plane cross section threaded by $B_{\parallel,1}$, which amounts to a plausible 10 nm. In particular, for the asymmetric SQUID transmon, this model fits the distinctive behavior of the individual JJs forming the SQUID loop [Fig. 3(d)]: the larger JJ shows a rapid decrease in E_J, followed by a slight upturn for $B_{\parallel,1} > 0.9$ T that is consistent with the emergence of a second Fraunhofer lobe. The smaller JJ, in turn, is less affected by flux penetration, and its E_J decreases slowly and monotonically. While full BCS modeling of the superconducting gap for the thin films could further improve the fits, it is clear that the junction geometry plays a role for conventional $Al/AlO_x/Al$ JJs also and should be considered when targeting them for operation in high magnetic fields. The overall JJ footprint should be small, and it should especially be narrow in the axis parallel to the magnetic field.

In Fig. 3(b), there is a gap in the SQUID data between 0.4 and 0.5 T, and the single-JJ data are more noisy in this area. In this region, no clear SQUID oscillations can be observed when $B_\perp$ is swept. Measurements of the cavity frequency as a function of $B_\perp$ are not reproducible, and the cavity frequency is stable only for several minutes, making qubit spectroscopy of both qubits challenging. However, the data points that could be gathered for the single-JJ transmon are generally consistent with the data outside this region. This instability can also be observed when we measure in the $B_{\parallel,2}$ direction, but it arises even at low fields around 20 mT. It is for this reason that we focus on the $B_{\parallel,1}$ direction here. Details of these instabilities for $B_{\parallel,1}$ and $B_{\parallel,2}$ can be found in Ref. [41]. We suspect that spurious JJs inherent in our simple fabrication procedure are

responsible; it would be beneficial to avoid them when exploring large magnetic fields [35].

Eventually, our measurements become limited by the decreasing signal-to-noise ratio as the dispersive shifts of the transmons become small. Therefore, we do not measure the single-JJ transmon at magnetic fields above 0.69 T. However, we can measure characteristic SQUID oscillations over the entire field range of 1 T that is available to us, as the distinctive frequency modulation helps to identify the SQUID-transmon transitions. Unfortunately, because the values of B_{Φ_0} for the SQUID junctions are above or close to $B_{\parallel}^{\mathrm{crit}}$, the upturn in E_{J1} for $B_{\parallel,1} > 0.9$ T is relatively weak.

V. IN-PLANE MAGNETIC FIELD DEPENDENCE OF THE COHERENCE TIMES

Now we turn from the energy spectrum of the transmons to the coherence as a function of $B_{\parallel,1}$. At each value of $B_{\parallel,1}$, data sets such as the one shown in Fig. 2 are taken. To eliminate the $B_\perp$ dependence, Figs. 4(a) and 4(b) show the highest 5% of all T_1, T_2^*, and T_2^{echo} measured at each $B_{\parallel,1}$. As seen in Fig. 2, the values of $B_\perp$ for the maximum T_1, T_2^*, and T_2^{echo} do not necessarily coincide.

We observe microsecond values of T_1 over the entire $B_{\parallel,1}$ range measurable in the time domain. While T_1 for the single-JJ transmon is essentially constant up to 0.4 T, T_1 for the SQUID transmon shows a slight improvement, with a maximum T_1 of more than 30 μs for $B_{\parallel,1} = 0.34$ T. At that point, the perpendicular field offset B_0 for the maximum T_1 coincides with the bottom sweet spot, and, as we noted earlier (see Sec. III), at the bottom sweet spot, T_1 is usually longer than that at the top sweet spot. A slight improvement in T_1 is also expected because the Purcell effect is reduced at higher fields and lower frequencies (see Appendix G). In the instability region between 0.4 and 0.5 T, the few data points for the single-JJ transmon (and one data point for the SQUID device) suggest a reduction in T_1. While T_1 for the single-JJ transmon stabilizes at a slightly lower 2–4 μs after the instability region, the dependence of T_1 for the SQUID transmon at high fields is less clear. We do not understand the sudden drop in T_1 for the SQUID transmon, nor the gradual improvement in T_1 that follows. From $B_{\parallel,1} > 0.65$ T onwards, we are unable to perform time-domain measurements at the bottom sweet spot, as the frequency becomes too low. Before that, our data represent the maximum T_1 across the entire SQUID oscillation; at the highest fields, we lose the lowest frequencies. Quasiparticle-induced decay does not seem to limit our transmons even for the highest magnetic fields, where the superconducting gap is smallest. For details, see Appendix G, where we compare our estimate of the closing of the superconducting gap (Sec. IV) with the qubit lifetimes at high $B_{\parallel,1}$.

We now discuss qubit dephasing. While, in general, microsecond coherence is maintained up to at least 0.7 T,

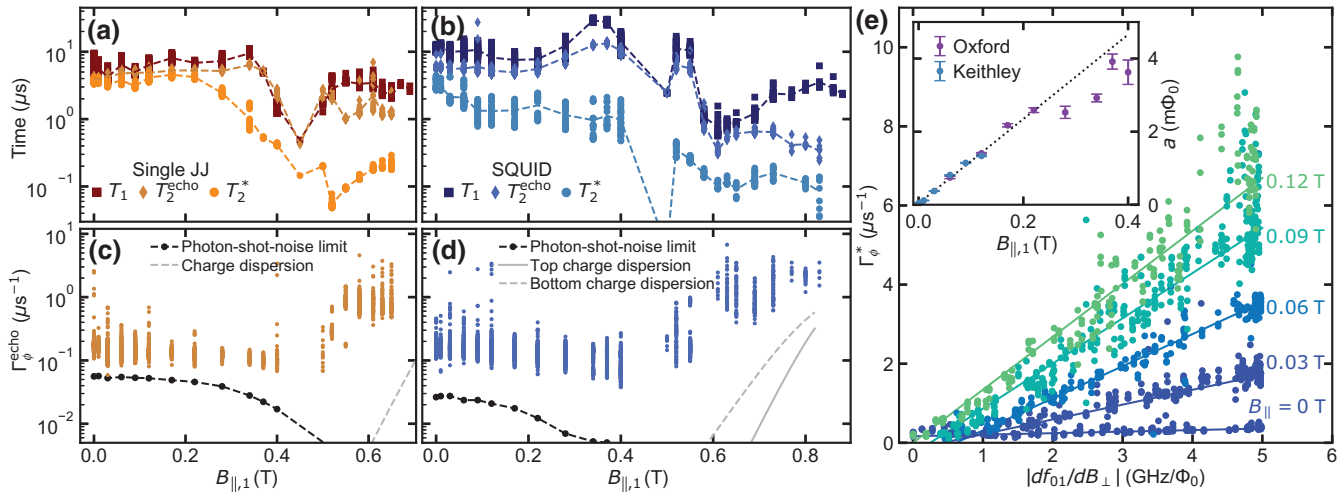

FIG. 4. Transmon qubit coherence as a function of $B_{\parallel,1}$. $B_\perp$ is varied at each $B_{\parallel,1}$, and we show the highest 5% of all T_1, T_2^{echo}, and T_2^* for (a) the single-JJ and (b) the SQUID transmon at each $B_{\parallel,1}$. The dashed lines indicate the mean of the high-coherence data at each field. Microsecond coherence is maintained up to at least 0.7 T, with T_1 above 1 μs over the entire measurable range. (c),(d) Pure echo dephasing rates $\Gamma_\phi^{\mathrm{echo}} = 1/T_2^{\mathrm{echo}} - 1/(2T_1)$ versus parallel magnetic field $B_{\parallel,1}$. For low magnetic fields (high frequencies), $\Gamma_\phi^{\mathrm{echo}}$ is limited by photon shot noise. For high magnetic fields, the transmons approach the low-E_J/E_C limit, and the charge dispersion $f_{01}(n_g = 0) - f_{01}(n_g = 0.5)$ increases, eventually limiting the coherence. (e) Pure Ramsey dephasing rate Γ_ϕ^* as a function of the SQUID frequency sensitivity $|df_{01}/dB_\perp|$. For every in-plane magnetic field $B_{\parallel,1}$, we observe a linear dependence $\Gamma_\phi^* = a\,|df_{01}/dB_\perp| + b$. The inset shows the slope a as a function of $B_{\parallel,1}$, which suggests that the noise in $B_\perp$ increases linearly with $B_{\parallel,1}$. The observed noise level and trend are independent of the current source connected to the $B_{\parallel,1}$ magnet coil (the current sources are denoted "Oxford" and "Keithley" in the legend). We believe that this noise is caused by mechanical vibrations (see text).

it is clear that T_2^{echo} is not T_1 limited. To better understand the limiting factors, we calculate the pure dephasing rate $\Gamma_\phi = 1/T_2 - 1/(2T_1)$ for both Ramsey and echo experiments. Figures 4(c) and 4(d) show $\Gamma_\phi^{\text{echo}}$ as a function of $B_{\parallel,1}$. Here we no longer restrict the discussion to the top 5% of the measured coherence times. Both devices show a qualitatively and quantitatively consistent trend: for in-plane magnetic fields up to 0.4 T, $\Gamma_\phi^{\text{echo}}$ shows a slight decrease, meaning improved coherence. We attribute this effect partially to photon shot noise in the cavity (see Appendix G), which limits the transmons less as their frequency decreases with increasing field (dashed line). The data suggest an effective cavity temperature of 76 mK, which is far above the dilution-refrigerator base temperature of approximately 10 mK. This could likely be improved by better shielding and filtering. For fields above 0.52 T, we observe increasing qubit dephasing, likely due to charge noise. The transmons approach the low-E_J/E_C limit, and the charge dispersion $f_{01}(n_g = 0) - f_{01}(n_g = 0.5)$ increases (dashed lines). Here n_g is the charge offset entering the Cooper-pair-box Hamiltonian (see Appendix E). With increasing charge dispersion, the transmons become proportionally more sensitive to charge noise [36].

As previously noted, the SQUID T_2^* shows a strong sweet-spot enhancement; we can therefore characterize the noise in $B_\perp$ as a function of $B_{\parallel,1}$ by performing a sensitivity analysis (see Appendix F). Here, the pure Ramsey dephasing Γ_ϕ^* is analyzed as a function of the SQUID frequency sensitivity $|df_{01}/dB_\perp|$ [Fig. 4(e)]. For every in-plane magnetic field $B_{\parallel,1}$, we observe a linear dependence $\Gamma_\phi^* = a\,|df_{01}/dB_\perp| + b$. The inset shows the slope a as a function of $B_{\parallel,1}$, which suggests that the noise in $B_\perp$ increases linearly with $B_{\parallel,1}$. The observed noise level and trend are independent of the current source powering the $B_{\parallel,1}$ magnet coil; we compare an Oxford Instruments Mercury iPS source with a low-noise Keithley current source (which cannot reach the currents required for higher fields). This suggests that the noise is not due to the current source for the $B_{\parallel,1}$ magnet. A possible explanation could be vibrations in the setup that convert $B_{\parallel,1}$ to $B_\perp$. Vibrations are usually low frequency, and the noise in $B_\perp$ would increase proportionally to $B_{\parallel,1}$. Γ_ϕ^* would be sensitive to this kind of low-frequency noise. We attempted to confirm this theory by measuring while turning off the pulse-tube cooler, which is likely the main source of vibrations in the dilution refrigerator, but turning it off leads to flux jumps, and we cannot recalibrate in the time the refrigerator stays cold.

A similar analysis is performed for the T_2^{echo} measurements, but $\Gamma_\phi^{\text{echo}}$ as a function of $|df_{01}/dB_\perp|$ is essentially flat, likely because it is limited mainly by photon shot noise or other noise sources that are not $B_\perp$ dependent (see Appendix G). Because of the asymmetry of the SQUID, $|df_{01}/dB_\perp|$ has an upper limit [44]; for a more symmetric SQUID, one could increase $|df_{01}/dB_\perp|$ until flux noise became a dominant noise source. The asymmetry is useful for extracting the magnetic field dependence of the individual JJs, but for studying flux noise, a symmetric SQUID would be beneficial. The fact that $\Gamma_\phi^{\text{echo}}$ does not show a strong $B_{\parallel,1}$ dependence is consistent with noise due to mechanical vibrations limiting Γ_ϕ^*, because mechanical vibrations are expected to be of low frequency and the noise can be largely echoed away. A similar situation is reported in Ref. [45].

VI. CONCLUSION

The present results show that for many applications in magnetic fields up to 0.4 T, the standard Al-AlO_x-Al JJs can be a viable option. In this regime, T_1 and T_2^{echo} remain largely unaffected in our transmons, but accurate in-plane alignment of the magnetic field is paramount for preserving coherence. We use thin aluminum films to increase the in-plane critical field and narrow leads to minimize vortex losses. For higher fields, the coherence times are reduced compared with the low-field levels, but the standard Al/AlO_x/Al transmon can be operated in magnetic fields up to 1 T, a value comparable to that for semiconductor nanowire transmons [31], while exhibiting better coherence times. For the $B_{\parallel,1}$ direction, the frequency dependence of the transmon is found to be reasonably well described by a simple model that considers a Fraunhofer-like geometrical contribution and the gap closing according to the Ginzburg-Landau theory. In addition, we show that the operation of a SQUID transmon is possible in high in-plane fields, although vibrations of the magnet relative to the sample and noise from the magnet current sources could become a limiting factor. These challenges seem solvable with better vibrational damping of the dilution refrigerator and the use of persistent-current magnets. However, between 0.4 and 0.5 T, regular SQUID oscillations cannot be observed, and the cavity frequency is unstable. We speculate that this is due to spurious JJs inherent in the Dolan-bridge fabrication process.

With thinner films and possibly a shift to a JJ fabrication process that minimizes spurious JJs, such as the use of Manhattan-style JJs [46] or JJs that are made in two lithography steps [47], it would be possible to make an Al-AlO_x-Al JJ transmon that can work above 1 T. If the target magnetic field is known in advance and the film properties are largely characterized, one can account for the reduction in E_J due to suppression of the superconducting gap. Then, the advantages of Al-AlO_x-Al JJs of high quality, reasonable yield, and targeting will remain available even in experiments that require high magnetic fields. In future, it would be interesting to look into charge-parity dynamics and thermal excitation in transmons at higher fields [48]. Strong in-plane magnetic fields present an additional tuning knob in cQED, which could help in understanding the physics of the coupling of quasiparticles

to a transmon. We also believe that, with slight improvements in the setup, it would be possible to measure the effect of magnetic fields on flux noise and shed light on the nature of the spin ensembles that are believed to cause this noise [49].

ACKNOWLEDGMENTS

We would like to thank Ida Milow for her internship in the laboratory and contributions to our code base. We thank T. Zent and L. Hamdan for technical assistance, and D. Fan for help with setting up the aluminum evaporator. We thank A. Salari, M. Rößler, S. Barzanjeh, M. Zemlicka, F. Hassani, and M. Peruzzo for contributions in the early stages of the experiments. This project has received funding from the European Research Council (ERC) under the European Union's Horizon 2020 research and innovation program (Grant Agreement No. 741121) and was also funded by the Deutsche Forschungsgemeinschaft (DFG, German Research Foundation) under CRC 1238 – 277146847 (Subproject B01), as well as under Germany's Excellence Strategy – Cluster of Excellence Matter and Light for Quantum Computing (ML4Q), EXC 2004/1 – 390534769.

APPENDIX A: DEVICE FABRICATION, GEOMETRY, AND FILM THICKNESS

The two transmon devices are standard 3D transmons with a Dolan-bridge JJ [40]. They are fabricated in a single electron-beam-lithography step and with double-shadow evaporation using a Plassys MEB 550S evaporator. The aluminum has 5N purity. To be able to mix and match, many transmons with varying JJ parameters are fabricated in the same run on a large sapphire piece and then diced. Thus, the two transmons in these experiments, while on two disconnected sapphire pieces, should have very similar properties of the aluminum film and the junctions. The JJ geometry of both transmons, with all relevant dimensions, can be seen in SEM images (Fig. 5). Because the taking of the SEM images alters or destroys the JJs, the actual devices are imaged after measurements are completed. In a junction test prior to the fabrication of the devices, the relative spread of the room-temperature resistances is on the order of 4%. We believe this to be largely due to the lithography rather than to film roughness or a nonuniform oxide layer. In the test, 79 out of 96 JJs are working, but we are limited by trying to make small JJs in order to obtain a large SQUID asymmetry. The reliability of our fabrication process is also confirmed by the fact that the critical current densities of the three junctions studied (proportional to the ratio of the E_J's in Table I over the junction areas obtained from Fig. 5) are approximately the same.

Crucially, the film thicknesses for the two evaporations are nominally 10 and 18 nm for the bottom and top layers, respectively. Reducing the film thickness further should be possible using the same evaporator. For previous devices with film thicknesses of 15 nm (bottom layer) and 30 nm (top layer), the in-plane critical field is on the order of 250–300 mT. In contrast, Al films of thickness $d \sim 7$ nm can remain superconducting up to 3 T [50]. As shown there, for this thickness the orbital effect of the parallel field and the Zeeman splitting contribute approximately equally to suppressing superconductivity. It is only for thicker films that one can use the relation [51]

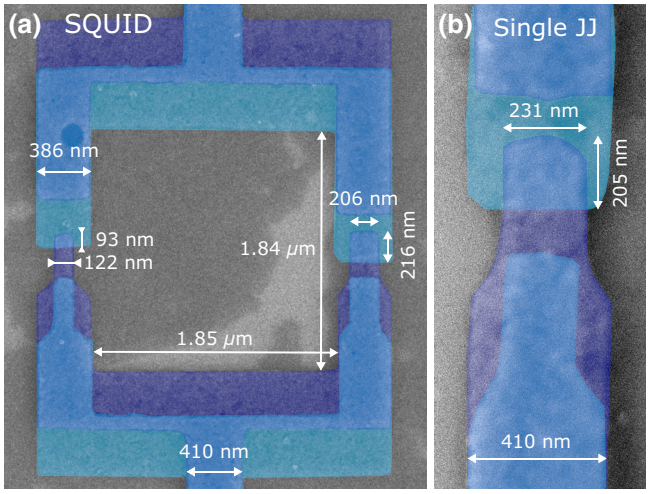

FIG. 5. False-color SEM images of (a) the SQUID loop of the SQUID transmon and (b) the single JJ of the single-JJ transmon. The bottom aluminum layer is overlaid with a turquoise layer, while the top layer is overlaid with a violet layer, leaving the overlap region colored blue. Measurements of the different dimensions are indicated (some taken from other images with greater resolution).

$$B_{\parallel}^{\mathrm{crit}} = B_c \frac{\sqrt{24}\lambda}{d}, \tag{A1}$$

where B_c is the thermodynamic critical field and λ is the (effective) penetration depth, which qualitatively explains the increase in critical field with decreasing thickness. Nonetheless, using the low-temperature value of the critical field for aluminum ($B_c = 10$ mT), estimating the mean free path ℓ to be of the order of the thickness, and using $\lambda \approx \lambda_L\sqrt{\xi_0/\ell}$, with the London penetration depth $\lambda_L = 16$ nm and the coherence length $\xi_0 = 1600$ nm, we obtain from Eq. (A1) an estimate $B_{\parallel}^{\mathrm{crit}} \approx 1$ T for the film of thickness $d = 10$ nm in our devices. For comparison, the same procedure for $d = 15$ and 30 nm gives $B_{\parallel}^{\mathrm{crit}} \approx 0.5$ and 0.2 T, compatible with our measurements.

We note that the numerical results for the order parameter presented in Ref. [50] can be well approximated, not too close to the parallel critical field, by the Ginzburg-Landau formula

$$\Delta(B_\parallel) = \Delta_0 \sqrt{1 - \left(\frac{B_\parallel}{B_\parallel^{\mathrm{crit}}}\right)^2}, \qquad \text{(A2)}$$

although with a (fitted) critical field larger than the one obtained numerically. While this justifies the phenomenological use of Eq. (A2) in analyzing the data, a further complication arises in our devices due to a proximity effect between two films of different thickness; however, modeling of this effect is beyond the scope of the present work.

APPENDIX B: ALIGNMENT OF MAGNETIC AXES WITH SAMPLE

Here we illustrate the alignment procedure for aligning our magnet axes precisely with the in-plane direction of our sample. We use the SQUID-oscillation offset as a signal to construct the two in-plane axes $B_{\parallel,1}$ and $B_{\parallel,2}$ from the physical magnet axes B_x, B_y, B_z. In our case, B_x for the magnet corresponds roughly to $B_\perp$. The current source connected to the B_x coil has a finer resolution and lower noise than the one connected to the B_y and B_z coils. We therefore use only the B_x coil to correct the extra out-of-plane field caused by B_y and B_z, and not vice versa. This is a simple rotation that we apply in software before setting the values.

To determine the alignment, we make a two-dimensional map of the cavity frequency as a function of B_x and B_y (or B_z). These measurements are fast, and we can scan the B_x field for several values of B_y with few visible jumps. The linear change in the offset of the SQUID oscillations along the B_x axis with changing B_y is due to an additional out-of-plane component of B_y. Then a linear fit is performed to find the misalignment, which is then corrected by an additional B_x field as a function of B_y. The resulting axis is our $B_{\parallel,1}$. An aligned data set can be seen in Fig. 6(a), a color plot of the cavity resonance frequency normalized line by line versus $B_\perp$ and $B_{\parallel,1}$. The stable offset of the oscillations over a large range of $B_{\parallel,1}$ suggests that we align our magnetic field axis to better than 0.05°. We determine the initial misalignment to be −0.61° between the B_y and $B_{\parallel,1}$ axes. For very low fields, there is usually a small deviation, which we attribute to small residual ferromagnetism in the vicinity of our sample being magnetized. A more concrete example, with misaligned and aligned data for the $B_{\parallel,2}$ direction, can be found in Ref. [41].

APPENDIX C: UNUSUAL $B_\perp$ DEPENDENCE OF T_1 AND THE MAXIMUM QUBIT FREQUENCY

The alignment of the magnet axes on the SQUID oscillations seems natural and gives a straightforward linear alignment procedure. While one would expect T_1 and the qubit frequency (meaning the superconducting gap) to be

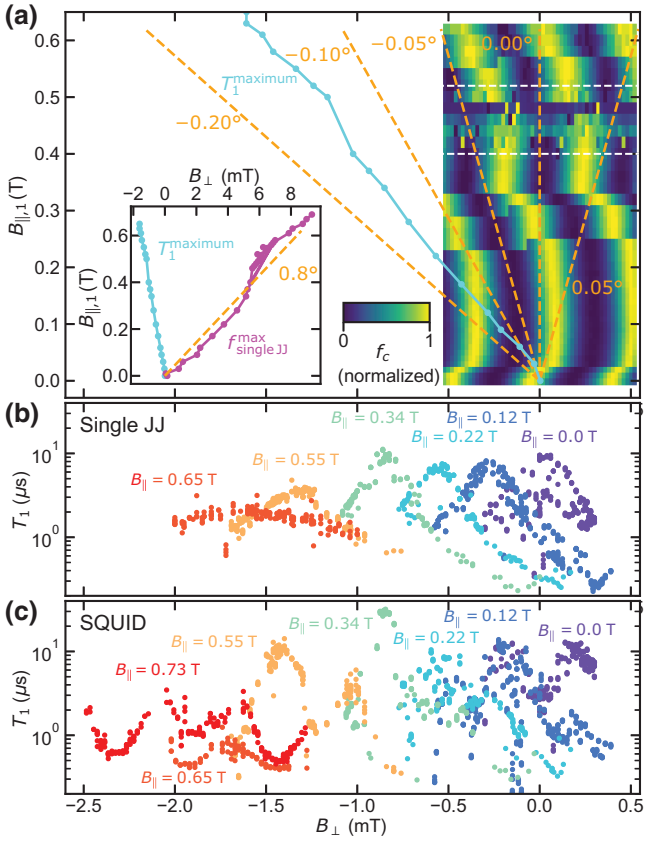

FIG. 6. (a) Cavity frequency (normalized line by line for contrast) as a function of $B_\perp$ and $B_{\parallel,1}$ (color plot). We observe clear SQUID oscillations in the cavity frequency, with a stable period for a large range of magnetic field. Occasional jumps can change the flux offset of the oscillations. The region between the two dashed white lines shows no stable SQUID oscillations. For perfect alignment, the oscillation offset should be constant for different values of $B_{\parallel,1}$. The orange dashed lines, corresponding to different angular misalignments, are given as a guide to the eye. We conclude that our alignment should be within ±0.05° with respect to the plane of the SQUID. The cyan line indicates the ($B_\perp$, $B_{\parallel,1}$) values corresponding to the maximum T_1 of the single-JJ transmon. The maximum T_1 values follow an axis at an angle of approximately −0.15° with respect to the sample plane. The inset additionally shows the ($B_\perp$, $B_{\parallel,1}$) values corresponding to the estimated maximum frequency of the single-JJ transmon (magenta), which follows an axis that is at an angle of approximately 0.8° with respect to the sample plane. (b),(c) Example data sets for T_1 as a function of $B_\perp$ for the single-JJ and the SQUID transmon, respectively, for different values of $B_{\parallel,1}$.

maximum at the nominal $B_\perp = 0$ (which depends on the alignment), we observe that they take their maximum values at finite values of $B_\perp$; furthermore, these values are different for the maximum T_1 and the maximum qubit frequency.

When looking at the $B_\perp$ corresponding to the largest T_1 at a given $B_{\parallel,1}$ for both transmons [Figs. 6(b) and 6(c)], we see that it deviates increasingly from $B_\perp = 0$. In the

following, we focus on the data for the single-JJ-transmon T_1, because these show more clear peaks, as there is no additional frequency dependence that complicates the picture. We designate the $B_\perp$ corresponding to the optimal T_1 as B_0. B_0 changes linearly with $B_{\parallel,1}$, such that we can estimate the angle with respect to the sample plane, which is roughly -0.15° [data labeled T_1^{maximum} in Fig. 6(a)]. The dependence of T_1 on $B_\perp$ is likely due to vortex creation, which takes place largely in the large capacitor pads. We show in Appendix D that, apart from this offset, it appears that the data are consistent with the vortex hypothesis. Initially, we believed that there could be hysteresis in the vortex system, which could lead to an offset in B_0. So, when changing $B_{\parallel,1}$, we try to scan $B_\perp$ back and forth, approaching the estimated $B_\perp = 0$ mT point, a procedure laid out in Ref. [52]. However, this procedure does not make a big difference. Some data on the hysteresis in $B_\perp$ at $B_{\parallel,1} = 0$ can be found in Ref [41], and while we see hysteresis in the SQUID offset and in the T_1 data, it is not necessarily identical. Ultimately, we find that B_0 seems to be stable for upward and downward scans in $B_{\parallel,1}$, and therefore it appears that hysteresis does not fully explain the effect. This effect could be investigated in more detail, e.g., we do not explore the negative direction in $B_{\parallel,1}$, but this is beyond the scope of the present work.

Peculiarly, the $B_\perp$ value corresponding to the maximum frequency of the single-JJ transmon seems also to deviate linearly from $B_\perp = 0$ at different values of $B_{\parallel,1}$, corresponding to an angle of 0.8° with respect to the in-plane direction [see inset of Fig. 6(a)]. Two example data sets for the frequency of the single-JJ transmon as a function of magnetic field are discussed in Appendix E. If one assumes that only E_J is field dependent, the maximum frequency corresponds to the maximum superconducting gap immediately at the JJ. Possibly due to flux focusing in the vicinity of the JJ, which has a step in the $B_{\parallel,1}$ direction, there is an additional angle with respect to the sample plane. While the differences in angle between the SQUID, the vortex system, and the maximum frequency of the single-JJ transmon are small in absolute terms, they are clearly distinguishable in our data.

APPENDIX D: VORTEX LOSS IN OUT-OF-PLANE MAGNETIC FIELDS

In Fig. 4, we plot the best T_1 as a function of $B_{\parallel,1}$; however, reaching the longest possible T_1 depends crucially on finding the appropriate $B_\perp$ value for a given $B_{\parallel,1}$, as we discuss in Appendix C, pointing to the possible role of vortices. Indeed, as shown both for resonators [53] and for transmons [43], the loss is proportional to the number of vortices; above a certain threshold field B_{th}, this number increases linearly with $B_\perp$. However, vortices can already enter the large transmon capacitor pads at fields smaller than B_{th} [53,54], leading to a more gradual onset of vortex

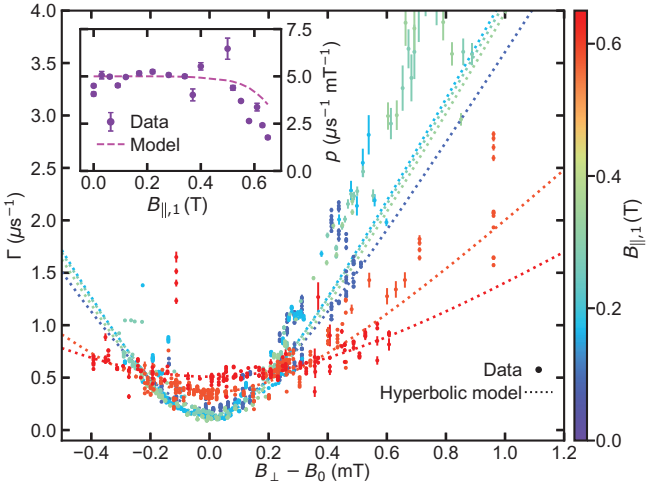

FIG. 7. Single-JJ-transmon relaxation rate $\Gamma = 1/T_1$ vs $B_\perp - B_0$ for various $B_{\parallel,1}$. The data are fitted using a phenomenological hyperbolic model [Eq. (D1)]. The inset shows the fitted asymptotic slope p of Eq. (D1). Interestingly, for $B_{\parallel,1} \geq 0.5$ T the slope shows a significant drop for high $B_{\parallel,1}$. We can model this decrease in p (dashed pink line), which we attribute mainly to the decreasing qubit frequency.

dissipation. To phenomenologically capture this behavior, we fit the vortex contribution to dissipation Γ_v with the formula

$$\Gamma_v = \sqrt{p^2 \tilde{B}_\perp^2 + q^2} - q, \tag{D1}$$

where p and q are fitting parameters, which we discuss below, and $\tilde{B}_\perp = B_\perp - B_0$, with the offset B_0 being the value of the perpendicular field where T_1 is largest for a given $B_{\parallel,1}$ (see Appendix C). We show in Fig. 7 the total relaxation rate $\Gamma = 1/T_1$ as a function of $B_\perp - B_0$ for several values of the parallel field; note that $\Gamma = \Gamma_0 + \Gamma_v$ includes also the nonvortex contribution Γ_0. Data over a wider range of perpendicular field, showing more clearly a regime of linear dependence of Γ_v on $B_\perp$, are reported in Ref. [41].

In fitting the data in Fig. 7, we fix $q = 1.3\ \mu\text{s}^{-1}$, while we treat p as a parallel field-dependent quantity. The inset in Fig. 7 presents the value of p as a function of $B_{\parallel,1}$; the coefficient p is the slope in the linear regime of Γ_v vs $B_\perp$. As discussed in Ref. [53], the value of the slope is affected by the so-called flux-flow viscosity η and the presence of pinning centers that can lead to vortex creep. Considering the model for the flow resistivity presented in Ref. [53] (see also [55]), we can write

$$p = p_0 \frac{1}{\sqrt{1 - (B_\parallel / B_\parallel^{\text{crit}})^2}} \frac{F(f(B_\parallel)/f_d, \epsilon)}{F(f(0)/f_d, \epsilon)}, \tag{D2}$$

where, by construction, p_0 is the slope at zero parallel field, $f(B_\parallel)$ is the transmon frequency as a function of

the parallel field, f_d is the depinning frequency, marking the crossover from an elastic to a viscous response of the vortices, and $0 \leq \epsilon \leq 1$ is the dimensionless creep parameter. For aluminum, the latter two quantities take the values $f_d = 4$ GHz and $\epsilon = 0.15$ [53]. The function F is defined as

$$F(x, \epsilon) = \frac{\epsilon + x^2}{1 + x^2}. \tag{D3}$$

Finally, the factor in the middle of Eq. (D2) arises as follows: the loss is inversely proportional to the viscosity η, and the latter is proportional to the upper critical field $B_{c2} = \Phi_0/(2\pi\xi^2)$, where $\xi \approx \sqrt{\hbar D/\Delta}$ is the coherence length in a disordered superconductor, with D being the diffusion constant (physically, the loss increases with the square of the coherence length because the latter determines the radius of the vortex core). Therefore, we expect $p \propto 1/\Delta(B_\parallel)$, a factor that we estimate using Eq. (A2).

The curve in the inset of Fig. 7 is plotted using Eq. (D2), with the qubit frequency obtained from the data in Fig. 3(b) and $B^{\text{crit}}_{\parallel,1} = 1.03$ T; see the caption of Table I. Hence $p_0 = 5\ \mu\text{s}^{-1}\ \text{mT}^{-1}$ is the only free parameter, which is fixed by fitting the data for $B_\parallel \leq 0.4$ T; for comparison, accounting for their different frequencies through the function F in Eq. (D3), the two qubits measured in Ref. [43] have $p_0 = 0.5$ and $1.2\ \mu\text{s}^{-1}\ \text{mT}^{-1}$. The curve captures the experimental drop of the slope with the parallel field, implying that the decrease in dissipation at low frequency due to pinning has a stronger effect than the increase due to the expansion of the vortex cores. Based on this result, we expect that by introducing pinning sites or vortex-trapping holes in the pads, the qubit can be made more robust to out-of-plane fields and less sensitive to misalignment, although care must be taken not to increase dielectric losses [56].

Returning now to Eq. (D1), the parameter q can be related to the threshold field by $B_{\text{th}} \sim q/p$; however, this identification is meaningful only at zero parallel field, since at higher fields (and hence lower frequencies) p is suppressed due to pinning. In this way, we estimate $B_{\text{th}} \sim q/p_0 \approx 0.26$ mT, which is similar to the value at which a decrease in T_1 starts in Ref. [43]. In that case, this value is related to the lower critical field for vortex entry into a region of the capacitor pads, close to the JJs, of lateral size approximately 10 μm. However, this explanation is not applicable to our device, since there are no features with comparable dimensions, and we expect vortex entry in the pads already at a few millitesla. We speculate that B_{th} could be related to the number of vortices exceeding the number of pinning sites. We do not expect vortices to enter the thin leads to the JJs in our device, because the lead width $w = 410$ nm is only a few times the coherence length $\xi \sim 0.85\sqrt{\xi_0 \ell} \approx 108$ nm (see Appendix A). In fact, an order-of-magnitude estimate of the field B_v for vortex entry into the leads applicable in the case $w \gg \xi$ is $B_v = \Phi_0/w^2 \approx 10$ mT [54]. Although the condition $w \gg \xi$ is not satisfied, this value suggests that vortices are not present in the leads in the few-millitesla range of perpendicular fields explored in this paper.

APPENDIX E: ESTIMATION OF E_J AND E_C FROM SPECTROSCOPY DATA

In Fig. 3, we show E_J as a function of $B_{\parallel,1}$. Here we want to elaborate on how we estimate E_J and E_C from the measured transmon spectrum. We also consider systematic errors, such as additional dependence on $B_\perp$ and cavity dressing.

E_J and E_C can be extracted from f_{01} and $f_{02}/2$ by fitting the measured transitions to a numerical Cooper-pair box Hamiltonian in the charge basis

$$H = 4E_C \sum_{n=-k}^{k} (n - n_g)^2 |n\rangle\langle n| + \frac{1}{2} E_J \sum_{n=-k}^{k} \left(|n\rangle\langle n+1| + |n+1\rangle\langle n|\right), \tag{E1}$$

with charge states $|n\rangle$, where n stands for the difference in the number of Cooper pairs between the two islands. A voltage gate or environmental noise can introduce a charge offset n_g. k is the truncation in the charge basis; we usually truncate at $k = 20$, and thus include 41 states. That way, we obtain accurate results in both the transmon regime and the low-E_J/E_C regime, where $f_{01} \approx \sqrt{8E_J E_C} - E_C$ stops being a good approximation. Every pair of f_{01} and $f_{02}/2$ measurements then gives a value for E_J and E_C. The data are shown in Fig. 8.

The data show a clear correlation between E_J and E_C because the participation of the cavity capacitance depends on the impedance matching between the cavity and transmon mode and therefore on E_J. The coupling between the cavity and the transmons is also not constant but depends on E_J and E_C. The dependence looks very similar for both transmons, and we can assume a linear dependence of E_C on E_J. The outliers in the data set can be due to a number of effects: bad peak fits (e.g., picking a wrong photon-number peak), flux or n_g jumps between the f_{01} and $f_{02}/2$ measurements, or hysteresis in the magnetic field. Throughout the experiment, we use continuous-wave spectroscopy. The powers are constantly adapted as the qubit-cavity detuning changes, trying to maintain a balance between visibility and minimizing the shifts due to the readout tone and the ac Stark shift.

Both the single-JJ- and the SQUID-transmon transitions vary with $B_\perp$. Furthermore, our large spectroscopy data set has outliers. As we sweep a small range in $B_\perp$ for every $B_{\parallel,1}$, we can identify and reject outliers easily. To obtain a robust estimate of $E_J(B_{\parallel,1})$, we do not extract all individual values for E_J from all pairs of f_{01} and $f_{02}/2$, but rather

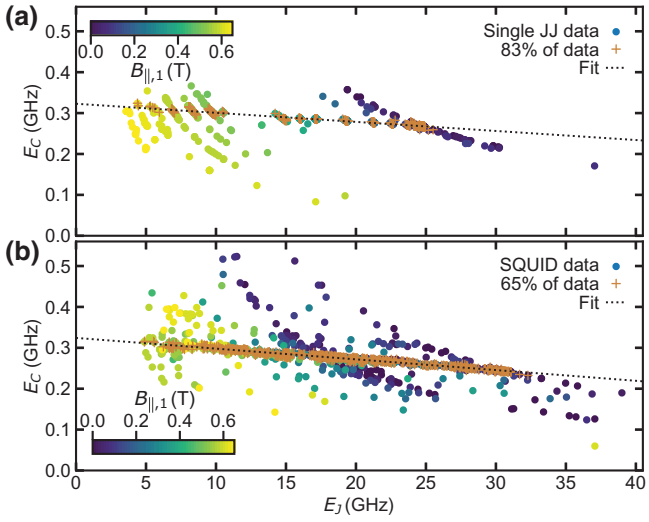

FIG. 8. E_C for (a) single-JJ and (b) SQUID transmon as a function of E_J. These data are extracted from pairwise spectroscopic measurements of f_{01} and $f_{02}/2$. For every pair, we fit the transitions to a numerical Cooper-pair box Hamiltonian, giving values for E_J and E_C (see text). We find a clear correlation of E_C and E_J: 65% of all SQUID data and 80% of all single-JJ-qubit data gather around a linear trend to within 10 MHz. The outliers can be due to a number of effects: bad peak fits (e.g., picking a wrong photon-number peak), or flux or n_g jumps between the f_{01} and $f_{02}/2$ measurements. By fitting a linear dependence, we can infer E_C from E_J.

fit a model to all transitions measured at a given $B_{\parallel,1}$ as a function of $B_\perp$. In the following, we give the models that we use for the $B_\perp$ dependence for the two transmons.

For the single-JJ transmon, the dependence on the out-of-plane field is dominated by a suppression of the superconducting gap. As in the case of the in-plane magnetic field, we model this dependence using the Ginzburg-Landau dependence of the gap on the field [51],

$$E_J(B_\perp) \propto \Delta(B_\perp) = \Delta(0)\sqrt{1-\left(\frac{B_\perp}{B_\perp^{\mathrm{crit}}}\right)^2}. \tag{E2}$$

Using the same form as in Eq. (A2) seems appropriate since, as discussed at the end of Appendix D, we do not expect vortices to play a role in the leads to the JJ, at least up to $B_\perp \sim 10$ mT, which covers the range of perpendicular fields in our measurements. Note that the critical field $B_\perp^{\mathrm{crit}}$ of the junction leads should not be confused with the upper critical field B_{c2} of the much wider pads introduced in Appendix D.

When an in-plane and an out-of-plane magnetic field are simultaneously applied, the effective $B_\perp^{\mathrm{crit}}(B_{\parallel,1})$ is reduced. In the Ginzburg-Landau theory for thin films, for any angle θ with respect to the film plane, the critical field $B^{\mathrm{crit}}(\theta)$ lies between $B_\perp^{\mathrm{crit}}$ and $B_{\parallel,1}^{\mathrm{crit}}$ and satisfies [51]

$$\left|\frac{B^{\mathrm{crit}}(\theta)\sin\theta}{B_\perp^{\mathrm{crit}}}\right| + \left(\frac{B^{\mathrm{crit}}(\theta)\cos\theta}{B_{\parallel,1}^{\mathrm{crit}}}\right)^2 = 1. \tag{E3}$$

Example data for the single-JJ-transmon transitions as a function of $B_\perp$ can be found in Fig. 9. We perform spectroscopy over a range of approximately 10 mT in $B_\perp$ at $B_{\parallel,1} = 0$ T and at $B_{\parallel,1} = 0.58$ T. At other fields, we generally measure a smaller range of approximately 2 mT in $B_\perp$ around the high-coherence interval, because we want mainly to make the case that high coherence can be maintained. But the frequency maximum as a function of $B_\perp$ for the single-JJ transmon increasingly deviates from the maximum coherence time (see Appendix C). In Fig. 9(b), the transmon frequency in the high-coherence interval around -1.5 mT is about 150 MHz lower than the maximum frequency that we measure. To account for this, we try to estimate the maximum E_J at every $B_{\parallel,1}$ by fitting all of the data available at different $B_\perp$ for each given $B_{\parallel,1}$. In the fit, we fix $B_\perp^{\mathrm{crit}}$ and $B_{\parallel,1}^{\mathrm{crit}}$ and use Eq. (E3) to extract the effective $B_\perp^{\mathrm{crit}}(B_{\parallel,1})$ for each $B_{\parallel,1}$. The free parameters are the maximum E_J, E_C, and the offset in $B_\perp$. For the highest

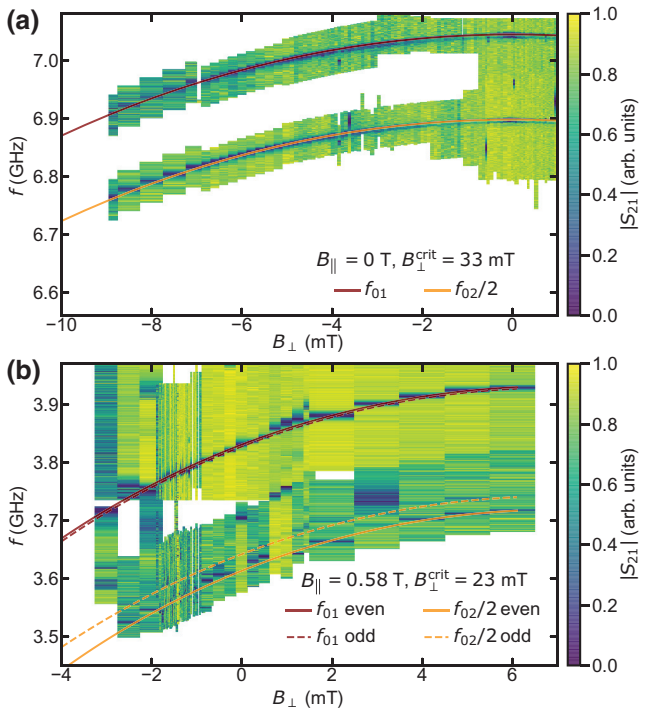

FIG. 9. Single-JJ-transmon f_{01} and $f_{02}/2$ as a function of $B_\perp$ for $B_{\parallel,1} = 0$ T (a) and for $B_{\parallel,1} = 0.58$ T (b). The data for (a) are taken in a previous cooldown in a different but nominally identical dilution refrigerator. We use these data to estimate $B_\perp^{\mathrm{crit}}$ using a fit of a simple Ginzburg-Landau model. The effective $B_\perp^{\mathrm{crit}}$ is lower in (b), as the superconductivity is also suppressed by the in-plane field.

fields, this suggests a correction of approximately +10% to E_J. Note that when we model the magnetic field dependence of the transmon frequencies, we consider the field dependence of E_J and therefore that of the superconducting gap right at the JJ. In fact, Eq. (E2) accounts for the gap suppression due to the perpendicular component of the field. This mechanism would result in the first term of Eq. (E3) being a square, like the second term, rather than an absolute value; the absolute value originates from the effect of vortices [51]. As we discuss, it is unclear what ultimately determines the perpendicular critical field in the leads, and hence which formulation is the correct one. In the measured range of parallel field, the two approaches give effective values of $B_\perp^{\text{crit}}$ differing by at most 25%, and so we opt to use the well-known Eq. (E3). In future experiments, this could be easily explored by measuring larger ranges of $B_\perp$ for each $B_{\parallel,1}$.

For the SQUID transmon, the effective E_J depends on $B_\perp$ and on the two individual Josephson energies E_{J1} and E_{J2} according to

$$E_J\left(B_\perp\right) = E_{J,\Sigma}\sqrt{\alpha_{\text{JJ}}^2 + \left(1-\alpha_{\text{JJ}}^2\right)\cos\left(\frac{\pi B_\perp}{B_{\Phi_0,\text{SQUID}}}\right)^2}, \tag{E4}$$

where $E_{J,\Sigma} = E_{J1} + E_{J2}$, the JJ asymmetry parameter is $\alpha_{\text{JJ}} = |E_{J1} - E_{J2}|/(E_{J1} + E_{J2})$, and the out-of-plane field $B_{\Phi_0,\text{SQUID}}$ corresponds to a flux quantum through the SQUID loop. Intuitively, the Josephson energies at the top (bottom) sweet spot correspond to the sum (difference) of the individual E_J's. Neglecting the suppression of the superconducting gap with $B_\perp$ that we note for the single-JJ transmon above, one can fit this dependence to a SQUID oscillation and get a result for E_{J1} and E_{J2}. In the fitting model, we use the linear relation of E_J and E_C extracted earlier (see Fig. 8). The suppression of the superconducting gap with $B_\perp$ can be neglected because of the large difference between $B_\perp^{\text{crit}} \approx 30$ mT and $B_{\Phi_0,\text{SQUID}} \approx 0.43$ mT. We also observe that the sweet-spot frequencies do not vary as strongly with $B_\perp$ as the frequency of the single-JJ transmon does.

Close to the cavity frequency, the anharmonicity of the transmon is modified by hybridization with the cavity. To estimate this effect and correct for it, we fit a two-qutrit–one-cavity Hamiltonian of the form

$$H = H_0 + H_{\text{coupling}} + H_{qq}. \tag{E5}$$

Here, H_0 is the uncoupled Hamiltonian for two qutrits and a resonator,

$$\begin{aligned} H_0 = {} & \hbar\omega_c a^\dagger a \\ & + \omega_{01,1}|1\rangle_1\langle 1|_1 + \omega_{02,1}|2\rangle_1\langle 2|_1 \\ & + \omega_{01,2}|1\rangle_2\langle 1|_2 + \omega_{02,2}|2\rangle_2\langle 2|_2, \end{aligned} \tag{E6}$$

where $\omega_c = 2\pi f_c$ is the cavity angular frequency, and a and $a^\dagger$ are creation and annihilation operators. H_{coupling} then models the qutrit-cavity interaction in the rotating-wave approximation, but avoiding the dispersive approximation:

$$\begin{aligned} H_{\text{coupling}} = {} & \hbar g_1\left[\left(|0\rangle_1\langle 1|_1 + \sqrt{2}|1\rangle_1\langle 2|_1\right)a + \text{c.c.}\right] \\ & + \hbar g_2\left[\left(|0\rangle_2\langle 1|_2 + \sqrt{2}|1\rangle_2\langle 2|_2\right)a + \text{c.c.}\right]. \end{aligned} \tag{E7}$$

Here, g_1 and g_2 denote the coupling strengths between the respective qutrit and the cavity. Finally, H_{qq} should be a direct qubit-qubit interaction. However, we measure the qubit-qubit avoided crossings at several fields and can bound the interaction to below 1 MHz. For the fit, we use only data away from the avoided crossing and neglect this term. Having a data set of dressed transitions ω_c, $\omega_{01}^{(q1)}$, $\omega_{02}^{(q1)}/2$, $\omega_{01}^{(q2)}$, and $\omega_{02}^{(q2)}/2$, we fit the respective energy levels of Eq. (E5) to these transitions [see Fig. 10(a)]. Approximating the bare cavity frequency by its high-power limit, $f_c = 8.107$ GHz, we obtain the cavity-qutrit couplings and bare qutrit frequencies. The couplings $g_{1,2}$ show a slight frequency dependence, which is expected as the transmon dipole moment is dependent on E_J and E_C [36]. In the range of the fit, we can make the approximation $g_{1,2}/2\pi = 57\,\text{MHz} + 0.01 f_{01}$, meaning that $g_{1,2}/2\pi$ ranges from 100 to 130 MHz. By refitting the estimated dependence of the bare SQUID frequency on $B_\perp$, we obtain more accurate values for E_J and E_C of the transmon. The bare and dressed values of E_C and E_J are compared in Figs. 10(b) and 10(c). The downward correction of E_J is less than 3%. With increasing field, the correction becomes even smaller, as the qubit frequencies and consequently the hybridization with the cavity mode decrease. The E_J presented in the main text is based on the bare levels when the transmon frequencies are close to that of the cavity.

For the highest fields, charge-parity splitting becomes a dominant effect in the transmon spectrum, as the E_J/E_C ratio becomes small. In spectroscopy, we observe peaks for the odd- and even-parity subspaces, and the charge offset n_g changes randomly. Example data sets and fits for single-JJ and SQUID qubits are shown in Figs. 11(a) and 11(b). The Hamiltonian remains the same as in Eq. (E1), but we evaluate it for $n_g = 0$ and $n_g = 0.5$ to have the two parity branches. The populations of those two states and the exact value of n_g are random, and drift. In order to extract E_J and E_C in this regime, we fit transitions obtained from the charge-parity-split Hamiltonian to bound the experimental data.

APPENDIX F: SENSITIVITY ANALYSIS OF NOISE IN $B_\perp$

Any noisy parameter that tunes the transmon frequency reduces the coherence of the transmon. The frequency of

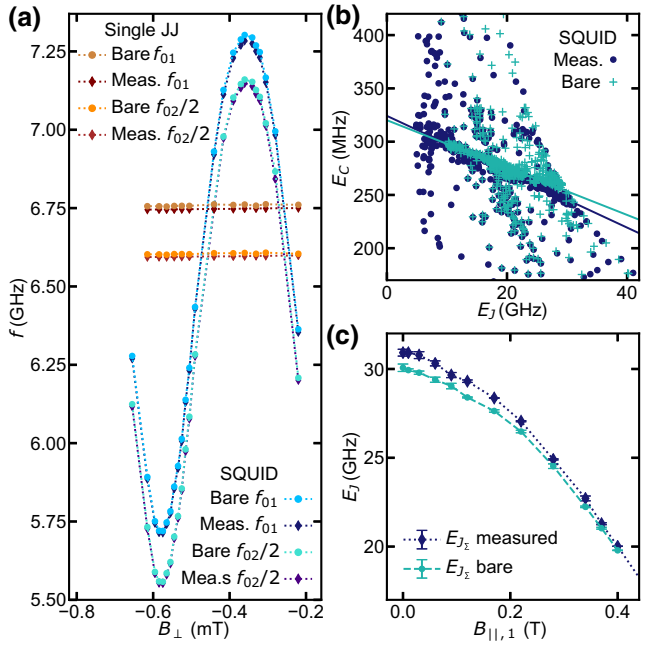

FIG. 10. Estimating bare transmon parameters. (a) By fitting a two-qutrit–one-cavity Hamiltonian to the measured frequencies, we can estimate the bare transmon frequencies. Closer to the cavity resonance frequency ($f_c = 8.1$ GHz), the hybridization is stronger, leading to a larger correction. (b) The E_C-E_J correlation, as described in Fig. 8, gives a slightly altered linear trend for the E_C obtained from the bare frequencies. (c) By refitting the estimated bare SQUID flux arches, we obtain a downward correction of E_J by 3%. With increasing field, the correction becomes smaller, as the qubit frequencies and consequently the hybridization with the cavity mode decrease.

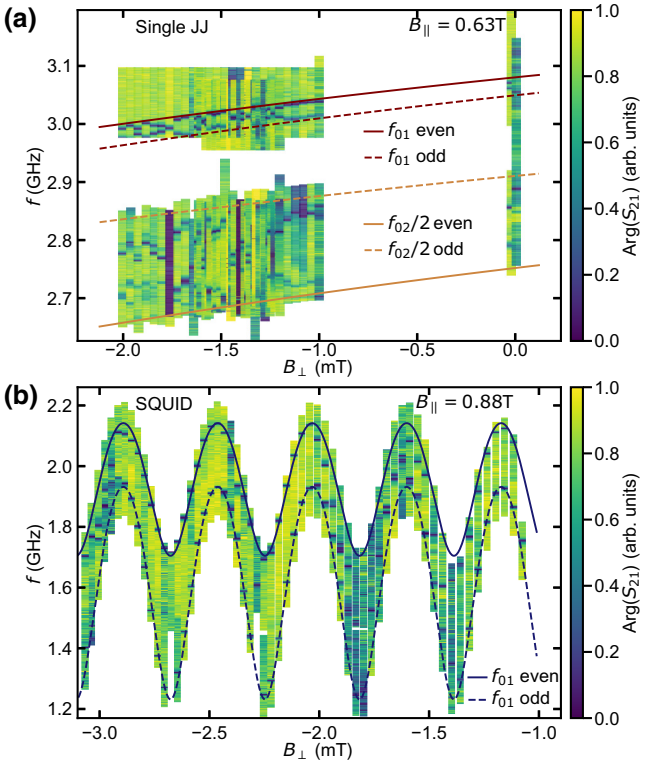

FIG. 11. Example data for extracting E_J and E_C from charge-parity splitting for (a) the single-JJ and (b) the SQUID transmon. Only the maximum splitting between the peaks needs to be estimated, as any value in between can be observed for a different n_g in the Hamiltonian. The changes in n_g that modulate the splitting happen on a timescale slower than the measurements, and therefore one can observe the opening and closing of the charge-parity splitting. For the single-JJ example, we can also observe $f_{02}/2$; for the SQUID example, we are in a regime where we can no longer observe $f_{02}/2$ and have to rely solely on f_{01}.

the SQUID transmon and therefore its coherence are sensitive to noise in the perpendicular magnetic field component $B_\perp$. This noise can be on-chip flux noise or setup-related, e.g., noise in the current source powering the magnet coils or vibrations of the sample with respect to the vector magnet. The sensitivity $|df_{01}/dB_\perp|$ determines the extent to which noise in $B_\perp$ reduces the transmon coherence. To calculate the sensitivity, we fit the flux dependence of the SQUID frequency using Eq. (E4). For every frequency, we calculate $|df_{01}/dB_\perp|$ from the fitted curve [Fig. 12(a)]. We can then plot $|df_{01}/dB_\perp|$ as a function of the SQUID transmon frequency f_{01} [Fig. 12(b)]. The main parameters that contribute to $|df_{01}/dB_\perp|$ as a function of frequency are the SQUID period $B_{\Phi_0,\mathrm{SQUID}}$ and the top and bottom sweet-spot frequencies (as well as E_C to a lesser degree). The sensitivity is given in units of GHz/Φ_0, because the fitted model also contains the periodicity in $B_\perp$, and thus we can rescale the x axis in units of Φ_0.

To quantify the transmon coherence, we calculate the pure dephasing time,

$$\frac{1}{T_2} = \Gamma_\phi + \frac{1}{2T_1}, \tag{F1}$$

to separate the contributions of the dephasing rate and the lifetime. Having measured T_1, T_2^*, and T_2^{echo} as a function of $B_\perp$ over at least one period of the SQUID, we can plot Γ_ϕ against $|df_{01}/dB_\perp|$. Figures 12(c) and 12(d) illustrate the case for Γ_ϕ^*, and Figs. 12(e) and 12(f) the case for $\Gamma_\phi^{\mathrm{echo}}$. We observe a linear dependence on the sensitivity

$$\Gamma_\phi = a\left|\frac{df_{01}}{dB_\perp}\right| + b, \tag{F2}$$

where a describes slow noise that scales with $B_\perp$, and the offset b accounts for flux-independent noise contributions. As illustrated in the four examples in Figs. 12(c)–12(f), we generally find such a linear trend for the Ramsey data, but not for the echo experiments, where we can see a clear difference between the high-frequency and low-frequency branches of the sensitivity. Therefore, it is only for Γ_ϕ^*

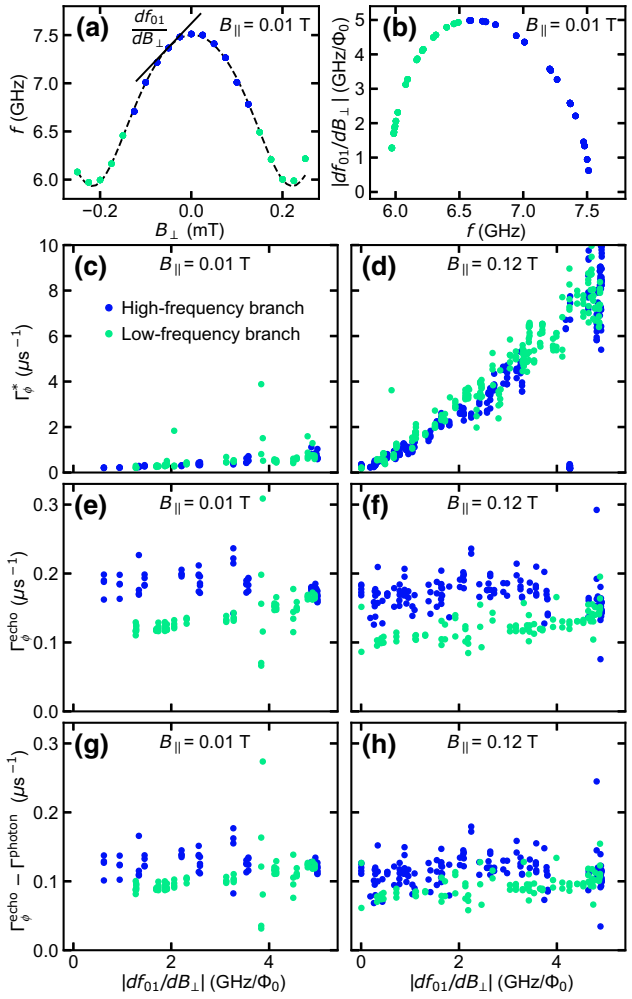

FIG. 12. (a) f_{01} of the SQUID qubit versus the out-of-plane field $B_\perp$ for an example flux oscillation of the SQUID at an in-plane field $B_{\parallel,1} = 0.01$ T. The tangent line indicates the sensitivity at that point. (b) Out-of-plane field sensitivity $|df_{01}/dB_\perp|$ as a function of frequency for the complete in-plane-field data set. The data in all figures are color coded to show the low-frequency and high-frequency sensitivity branches. (c),(d) Pure Ramsey dephasing rates of the SQUID qubit as a function of $|df_{01}/dB_\perp|$ at $B_{\parallel,1} = 0.01$ T and $B_{\parallel,1} = 0.12$ T. (e),(f) Pure echo dephasing rates of the SQUID qubit as a function of $|df_{01}/dB_\perp|$ at $B_{\parallel,1} = 0.01$ T and $B_{\parallel,1} = 0.12$ T. (g),(h) Pure echo dephasing rates of the SQUID qubit after subtracting our estimate of the photon shot noise as a function of $|df_{01}/dB_\perp|$ at $B_{\parallel,1} = 0.01$ T and $B_{\parallel,1} = 0.12$ T.

that we can extract the noise parameters a and b for each in-plane magnetic field and analyze them as a function of $B_{\parallel,1}$. The results for a are shown and discussed in Sec. V.

Compared with the Ramsey experiments, $\Gamma_\phi^{\text{echo}}$ should be more robust against low-frequency noise and give insights into faster noise such as on-chip flux noise, as opposed to slow setup-related vibrational noise. However, as shown in Appendix G, the echo dephasing rates are partially limited by photon shot noise in the cavity, which is strongly frequency dependent. Assuming this photon-shot-noise contribution, we subtract it as a frequency-dependent background. With this background subtraction, the gap between the upper and lower sensitivity branches (which differ in frequency) is reduced, as seen in Figs. 12(g) and 12(h). For the Ramsey data, the two branches of the sensitivity are consistent with the same linear trend to begin with, because the noise in $B_\perp$ limits Γ_ϕ^* more strongly. However, the photon-shot-noise-subtracted $\Gamma_\phi^{\text{echo}}$ becomes relatively flat, and so there is likely another $B_\perp$-independent noise source limiting $\Gamma_\phi^{\text{echo}}$. There is also no strong change in $\Gamma_\phi^{\text{echo}}$ as a function of $B_{\parallel,1}$ until we reach fields where the values also become more charge sensitive. Thus our data cannot give information about the characteristic $1/f$-like flux noise that is ubiquitous in cQED [49,57]. If this noise originates from local paramagnetic fluctuators, it is expected to depend on the applied magnetic field [45], and therefore repeating this experiment with improved coherence times could give insights into this.

APPENDIX G: ADDITIONAL RELEVANT LIMITS ON COHERENCE

Here, we present our understanding of additional relevant limits on the relaxation time and coherence of the transmons in the present work. While the qubits do not reach the current state of the art in terms of coherence time, this is likely largely due to insufficient shielding and filtering (see Ref. [41]). We discuss the Purcell and quasiparticle limits on T_1 and show evidence that T_2^{echo} is limited by photon shot noise. In the main text, we already discuss mechanical vibrations as a likely culprit limiting T_2^* at high $B_{\parallel,1}$. Vortex loss is discussed in Appendix D. We do not discuss the limits imposed on qubit dephasing by charge noise and quasiparticle dynamics in more detail in this paper, but they might be different from those for transmons with thicker aluminum films.

1. Limits on T_1

An important factor to consider in the qubit energy relaxation is the frequency. Figure 13 shows all measured T_1 values as a function of frequency for both qubits. There are several frequency-dependent mechanisms limiting T_1. The Purcell effect imposes a limit based on the coupling to the readout cavity, $T_1^{\text{Purcell}} = \delta^2/(g^2\kappa)$, where $\delta = f_{01} - f_c$ is the detuning between the qubit and the cavity mode, g is the qubit-cavity coupling, and κ is the cavity linewidth. Instead of κ, the quality factor $Q_{\text{tot}} = 2\pi f_c/\kappa$ is often quoted. We find $Q_{\text{tot}} \approx 5800$ at low fields, but at $B_{\parallel,1} \geq 0.5$ T we find $Q_{\text{tot}} \approx 3800$. Surprisingly, the measured f_c and Q_{tot} together with our estimates for g give a Purcell limit that some of our measured T_1 values exceed. Over a larger range, transmons limited by dielectric loss

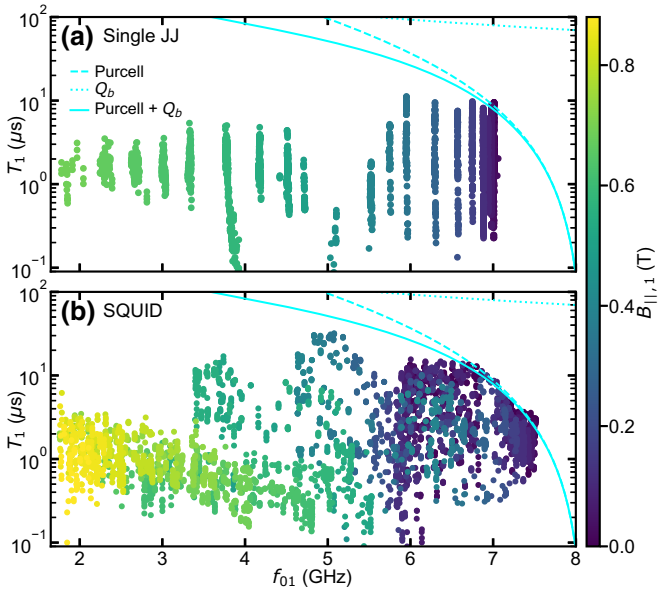

FIG. 13. T_1 versus transmon f_{01} for every in-plane magnetic field for both (a) the single-JJ and (b) the SQUID transmon. Purcell decay to the cavity mode limits both qubits at high frequencies. For similar frequencies but different values of $B_{\parallel,1}$, the single-JJ and SQUID transmons show very different features, e.g., a dip and a peak around 5.0 GHz. The observed lifetimes do not follow a frequency-dependent loss model, contrary to Ref. [29].

often exhibit an overall trend in T_1 that roughly follows the form ${T_1}^b = Q_b/2\pi f_{01}$, where Q_b is a background quality factor [58]. We cannot observe such a trend convincingly, but include it in Fig. 13 as a guide to the eye, setting $Q_b = 3.5 \times 10^6$.

As the magnetic field suppresses the superconducting gap, it is important to consider quasiparticle-induced relaxation. To estimate this effect, the superconducting gap needs to be estimated in absolute terms. As discussed in Sec. IV, we estimate the in-plane critical field to be $B_\parallel^{\text{crit}} = 1.03$ T. Assuming a Ginzburg-Landau closing of the superconducting gap [Eq. (A2)], we find the gap to be reduced by only approximately 50% at $B_{\parallel,1} = 0.88$ T. The data taken during the cooldown suggest $T_{\text{crit}} \approx 1.2$ K, which we can use to estimate the gap at zero magnetic field via $\Delta_0 = 1.764\, k_B T_{\text{crit}}$ [51,59]. With these values, we can calculate an estimate for the quasiparticle-induced relaxation rate [60]

$$\Gamma_{qp} = 2\frac{8E_J E_C x_{qp}}{f_{01}}\sqrt{\frac{2\Delta}{hf_{01}}}, \tag{G1}$$

where

$$x_{qp} = \sqrt{2\pi\frac{k_B T_R}{\Delta}}\exp\left(-\frac{\Delta}{k_B T_{\text{R}}}\right) \tag{G2}$$

is the normalized quasiparticle density, assuming a thermal-equilibrium temperature T_R. Here, h is the Planck constant and k_B is the Boltzmann constant. The remaining free parameter is the quasiparticle bath temperature T_R. At 0.88 T, we measure a T_1 of 2.4 μs for the SQUID transmon, which has a frequency of 1.8 GHz. With these values, we can roughly bound T_R to be less than or equal to 90 mK. More importantly, we do not observe any sharp decrease in T_1 with $B_{\parallel,1}$ that would signal this loss mechanism becoming dominant [29]. This suggests that, up to the highest field that we measure, T_1 is not significantly limited by quasiparticles.

2. Limits on T_2

Turning to the echo coherence times T_2^{echo}, we now estimate the limit imposed by photon shot noise in the cavity. As can be seen in Fig. 4, $\Gamma_\phi^{\text{echo}}$ decreases slightly with $B_{\parallel,1}$ for $B_{\parallel,1} < 400$ mT. Looking at $\Gamma_\phi^{\text{echo}}$ as a function of the qubit frequency (Fig. 14) is more revealing in this context. A dependence on the qubit frequency is expected using a model for photon shot noise [38,61]. In the dispersive limit, the qubit-cavity interaction is reduced to a term of the form $\chi a^\dagger a \sigma_z$. Accordingly, the qubit frequency depends on the cavity photon number $a^\dagger a$ via the dispersive shift χ, which for a transmon is given by

$$\chi = g^2\alpha_{\text{tr}}\left[\frac{1}{\delta(\delta+\alpha_{\text{tr}})} - \frac{1}{(\delta-2f_{01})(\delta-\alpha_{\text{tr}}-2f_{01})}\right], \tag{G3}$$

where $\alpha_{\text{tr}} = f_{12} - f_{01}$ is the negative transmon anharmonicity. Thus, thermal fluctuations in the cavity photon number lead to a dephasing rate

$$\Gamma^{\text{photon}} = \frac{\kappa}{2}\text{Re}\left[\sqrt{\left(1+\frac{2i\chi}{\kappa}\right)^2 + \left(\frac{8i\chi n_{\text{th}}}{\kappa}\right)} - 1\right]. \tag{G4}$$

The thermal cavity photon number $n_{\text{th}} = [\exp(hf_c/k_B T_{\text{cav}}) - 1]^{-1}$ is given by Bose-Einstein statistics. The only free parameter is the cavity temperature T_{cav}. As the photon-shot-noise limit on T_2^{echo} depends mainly on the transmon frequency, we show $\Gamma_\phi^{\text{echo}}$ versus f_{01} for both transmons in Fig. 14. Using $T_{\text{cav}} = 76$ mK, we can approximately reproduce the smallest $\Gamma_\phi^{\text{echo}}$ we measured for the single-JJ transmon. This data point is admittedly an outlier, but the underlying measurements of both T_1 and T_2^{echo} have good signal-to-noise ratios and fits; however, T_1 could have fluctuated. In that case, the photon shot noise would likely be more severe. Even with this low estimate, at qubit frequencies above 5 GHz, photon shot noise is a significant contribution to T_2^{echo}.

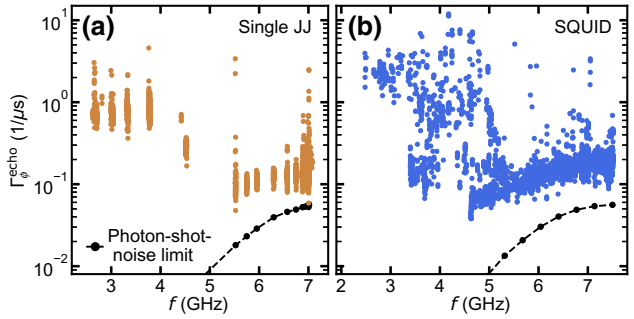

FIG. 14. (a) Pure echo dephasing rate of the single-JJ transmon against the transmon transition frequency. The black circles model photon shot noise with $T_{cav} = 76$ mK. (b) Similar to (a), but for the SQUID transmon.

[1] A. Blais, R.-S. Huang, A. Wallraff, S. M. Girvin, and R. J. Schoelkopf, Cavity quantum electrodynamics for superconducting electrical circuits: An architecture for quantum computation, Phys. Rev. A **69**, 062320 (2004).

[2] V. Ambegaokar and A. Baratoff, Tunneling between Superconductors, Phys. Rev. Lett. **10**, 486 (1963).

[3] J. M. Kreikebaum, K. P. O'Brien, A. Morvan, and I. Siddiqi, Improving wafer-scale Josephson junction resistance variation in superconducting quantum coherent circuits, Supercond. Sci. Technol. **33**, 06LT02 (2020).

[4] N. Muthusubramanian, A. Bruno, B. Tarasinski, A. Fognini, R. Hagen, L. Dicarlo, and N. M. Team, in *APS March Meeting Abstracts*, Vol. 2019 (2019), p. B29.

[5] J. B. Hertzberg, E. J. Zhang, S. Rosenblatt, E. Magesan, J. A. Smolin, J.-B. Yau, V. P. Adiga, M. Sandberg, M. Brink, and J. M. Chow, *et al.*, Laser-annealing Josephson junctions for yielding scaled-up superconducting quantum processors, npj Quantum Inf. **7**, 1 (2021).

[6] F. Arute, K. Arya, R. Babbush, D. Bacon, J. C. Bardin, R. Barends, R. Biswas, S. Boixo, F. G. Brandao, and D. A. Buell, *et al.*, Quantum supremacy using a programmable superconducting processor, Nature **574**, 505 (2019).

[7] C. Macklin, K. O'Brien, D. Hover, M. E. Schwartz, V. Bolkhovsky, X. Zhang, W. D. Oliver, and I. Siddiqi, A near–quantum-limited Josephson traveling-wave parametric amplifier, Science **350**, 307 (2015).

[8] A. Clerk, K. Lehnert, P. Bertet, J. Petta, and Y. Nakamura, Hybrid quantum systems with circuit quantum electrodynamics, Nat. Phys. **16**, 257 (2020).

[9] J. Clarke and A. I. Braginski, *The SQUID Handbook: Applications of SQUIDs and SQUID Systems* (John Wiley & Sons, Weinheim, Germany, 2006).

[10] L. DiCarlo, J. M. Chow, J. M. Gambetta, L. S. Bishop, B. R. Johnson, D. I. Schuster, J. Majer, A. Blas, S. M. Frunzio, L. an Girvin, and R. J. Schoelkopf, Demonstration of two-qubit algorithms with a superconducting quantum processor, Nature **460**, 240 (2009).

[11] Y. Chen, *et al.*, Qubit Architecture with High Coherence and Fast Tunable Coupling, Phys. Rev. Lett. **113**, 220502 (2014).

[12] M. Reagor, C. B. Osborn, N. Tezak, A. Staley, G. Prawiroatmodjo, M. Scheer, N. Alidoust, E. A. Sete, N. Didier, and M. P. da Silva, *et al.*, Demonstration of universal parametric entangling gates on a multi-qubit lattice, Sci. Adv. **4**, eaao3603 (2018).

[13] L. Chen, W. Wernsdorfer, C. Lampropoulos, G. Christou, and I. Chiorescu, On-chip squid measurements in the presence of high magnetic fields, Nanotechnology **21**, 405504 (2010).

[14] B. Schneider, S. Etaki, H. Van Der Zant, and G. Steele, Coupling carbon nanotube mechanics to a superconducting circuit, Sci. Rep. **2**, 1 (2012).

[15] K. E. Khosla, M. R. Vanner, N. Ares, and E. A. Laird, Displacemon Electromechanics: How to Detect Quantum Interference in a Nanomechanical Resonator, Phys. Rev. X **8**, 021052 (2018).

[16] I. Rodrigues, D. Bothner, and G. Steele, Coupling microwave photons to a mechanical resonator using quantum interference, Nat. Commun. **10**, 1 (2019).

[17] M. Kounalakis, Y. M. Blanter, and G. A. Steele, Synthesizing multi-phonon quantum superposition states using flux-mediated three-body interactions with superconducting qubits, npj Quantum Inf. **5**, 1 (2019).

[18] P. Schmidt, M. T. Amawi, S. Pogorzalek, F. Deppe, A. Marx, R. Gross, and H. Huebl, Sideband-resolved resonator electromechanics based on a nonlinear Josephson inductance probed on the single-photon level, Commun. Phys. **3**, 1 (2020).

[19] T. Bera, S. Majumder, S. K. Sahu, and V. Singh, Large flux-mediated coupling in hybrid electromechanical system with a transmon qubit, Commun. Phys. **4**, 1 (2021).

[20] T. Luschmann, P. Schmidt, F. Deppe, A. Marx, A. Sanchez, R. Gross, and H. Huebl, Mechanical frequency control in inductively coupled electromechanical systems, Sci. Rep. **12**, 1608 (2022).

[21] N. Samkharadze, G. Zheng, N. Kalhor, D. Brousse, A. Sammak, U. C. Mendes, A. Blais, G. Scappucci, and L. M. K. Vandersypen, Strong spin-photon coupling in silicon, Science **359**, 1123 (2018).

[22] X. Mi, M. Benito, S. Putz, D. M. Zajac, J. M. Taylor, G. Burkard, and J. R. Petta, A coherent spin–photon interface in silicon, Nature **555**, 599 (2018).

[23] R. M. Lutchyn, J. D. Sau, and S. Das Sarma, Majorana Fermions and a Topological Phase Transition in Semiconductor-Superconductor Heterostructures, Phys. Rev. Lett. **105**, 077001 (2010).

[24] A. Cook and M. Franz, Majorana fermions in a topological-insulator nanowire proximity-coupled to an *s*-wave superconductor, Phys. Rev. B **84**, 201105(R) (2011).

[25] F. Hassler, A. R. Akhmerov, and C. W. J. Beenakker, The top-transmon: A hybrid superconducting qubit for parity-protected quantum computation, New J. Phys. **13**, 095004 (2011).

[26] N. Samkharadze, A. Bruno, P. Scarlino, G. Zheng, D. P. DiVincenzo, L. DiCarlo, and L. M. K. Vandersypen, High-Kinetic-Inductance Superconducting Nanowire Resonators for Circuit qed in a Magnetic Field, Phys. Rev. Appl. **5**, 044004 (2016).

[27] J. G. Kroll, F. Borsoi, K. L. van der Enden, W. Uilhoorn, D. de Jong, M. Quintero-Pérez, D. J. van Woerkom, A. Bruno,

S. R. Plissard, D. Car, E. P. A. M. Bakkers, M. C. Cassidy, and L. P. Kouwenhoven, Magnetic-Field-Resilient Superconducting Coplanar-Waveguide Resonators for Hybrid Circuit Quantum Electrodynamics Experiments, Phys. Rev. Appl. **11**, 064053 (2019).

[28] K. Borisov, D. Rieger, P. Winkel, F. Henriques, F. Valenti, A. Ionita, M. Wessbecher, M. Spiecker, D. Gusenkova, and I. Pop, *et al.*, Superconducting granular aluminum resonators resilient to magnetic fields up to 1 tesla, Appl. Phys. Lett. **117**, 120502 (2020).

[29] F. Luthi, T. Stavenga, O. W. Enzing, A. Bruno, C. Dickel, N. K. Langford, M. A. Rol, T. S. Jespersen, J. Nygård, P. Krogstrup, and L. DiCarlo, Evolution of Nanowire Transmon Qubits and Their Coherence in a Magnetic Field, Phys. Rev. Lett. **120**, 100502 (2018).

[30] M. Pita-Vidal, A. Bargerbos, C.-K. Yang, D. J. van Woerkom, W. Pfaff, N. Haider, P. Krogstrup, L. P. Kouwenhoven, G. de Lange, and A. Kou, Gate-Tunable Field-Compatible Fluxonium, Phys. Rev. Appl. **14**, 064038 (2020).

[31] A. Kringhøj, T. W. Larsen, O. Erlandsson, W. Uilhoorn, J. G. Kroll, M. Hesselberg, R. P. G. McNeil, P. Krogstrup, L. Casparis, C. M. Marcus, and K. D. Petersson, Magnetic-Field-Compatible Superconducting Transmon Qubit, Phys. Rev. Appl. **15**, 054001 (2021).

[32] J. G. Kroll, W. Uilhoorn, K. L. van der Enden, D. de Jong, K. Watanabe, T. Taniguchi, S. Goswami, M. C. Cassidy, and L. P. Kouwenhoven, Magnetic field compatible circuit quantum electrodynamics with graphene Josephson junctions, Nat. Commun. **9**, 1 (2018).

[33] P. Winkel, K. Borisov, L. Grünhaupt, D. Rieger, M. Spiecker, F. Valenti, A. V. Ustinov, W. Wernsdorfer, and I. M. Pop, Implementation of a Transmon Qubit Using Superconducting Granular Aluminum, Phys. Rev. X **10**, 031032 (2020).

[34] M. Mergenthaler, A. Nersisyan, A. Patterson, M. Esposito, A. Baumgartner, C. Schönenberger, G. A. D. Briggs, E. A. Laird, and P. J. Leek, Circuit Quantum Electrodynamics with Carbon-Nanotube-Based Superconducting Quantum Circuits, Phys. Rev. Appl. **15**, 064050 (2021).

[35] A. Schneider, T. Wolz, M. Pfirrmann, M. Spiecker, H. Rotzinger, A. V. Ustinov, and M. Weides, Transmon qubit in a magnetic field: Evolution of coherence and transition frequency, Phys. Rev. Res. **1**, 023003 (2019).

[36] J. Koch, T. M. Yu, J. Gambetta, A. A. Houck, D. I. Schuster, J. Majer, A. Blais, M. H. Devoret, S. M. Girvin, and R. J. Schoelkopf, Charge-insensitive qubit design derived from the cooper pair box, Phys. Rev. A **76**, 042319 (2007).

[37] H. Paik, D. I. Schuster, L. S. Bishop, G. Kirchmair, G. Catelani, A. P. Sears, B. R. Johnson, M. J. Reagor, L. Frunzio, L. I. Glazman, S. M. Girvin, M. H. Devoret, and R. J. Schoelkopf, Observation of High Coherence in Josephson Junction Qubits Measured in a Three-Dimensional Circuit qed Architecture, Phys. Rev. Lett. **107**, 240501 (2011).

[38] C. Rigetti, J. M. Gambetta, S. Poletto, B. L. T. Plourde, J. M. Chow, A. D. Córcoles, J. A. Smolin, S. T. Merkel, J. R. Rozen, G. A. Keefe, M. B. Rothwell, M. B. Ketchen, and M. Steffen, Superconducting qubit in a waveguide cavity with a coherence time approaching 0.1 ms, Phys. Rev. B **86**, 100506(R) (2012).

[39] A. A. Abdumalikov Jr, J. M. Fink, K. Juliusson, M. Pechal, S. Berger, A. Wallraff, and S. Filipp, Experimental realization of non-abelian non-adiabatic geometric gates, Nature **496**, 482 (2013).

[40] G. J. Dolan, Offset masks for lift-off photoprocessing, Appl. Phys. Lett. **31**, 337 (1977).

[41] The supplemental material at http://link.aps.org/supplemental/10.1103/PhysRevApplied.17.034032 provides experimental details and additional data supporting the claims in the main text by additionally citing Refs. [62–68].

[42] C. Wang, Y. Y. Gao, I. M. Pop, U. Vool, C. Axline, T. Brecht, R. W. Heeres, L. Frunzio, M. H. Devoret, and G. Catelani, *et al.*: Measurement and control of quasiparticle dynamics in a superconducting qubit, Nat. Commun. **5**, 1 (2014).

[43] J. Ku, Z. Yoscovits, A. Levchenko, J. Eckstein, and A. Bezryadin, Decoherence and radiation-free relaxation in meissner transmon qubit coupled to abrikosov vortices, Phys. Rev. B **94**, 165128 (2016).

[44] M. D. Hutchings, J. B. Hertzberg, Y. Liu, N. T. Bronn, G. A. Keefe, M. Brink, J. M. Chow, and B. L. T. Plourde, Tunable Superconducting Qubits with Flux-Independent Coherence, Phys. Rev. Appl. **8**, 044003 (2017).

[45] F. Lüthi, *Circuit Quantum Electrodynamics in a Magnetic Field*, Ph.D. thesis, school Delft University of Technology (2019).

[46] A. Potts, G. Parker, J. Baumberg, and P. de Groot, Cmos compatible fabrication methods for submicron Josephson junction qubits, IEE Proc.-Sci., Meas. Technol. **148**, 225 (2001).

[47] X. Wu, J. L. Long, H. S. Ku, R. E. Lake, M. Bal, and D. P. Pappas, Overlap junctions for high coherence superconducting qubits, Appl. Phys. Lett. **111**, 032602 (2017).

[48] W. Uilhoorn, J. G. Kroll, A. Bargerbos, S. D. Nabi, C.-K. Yang, P. Krogstrup, L. P. Kouwenhoven, A. Kou, and G. de Lange, Quasiparticle trapping by orbital effect in a hybrid superconducting-semiconducting circuit, (2021), ArXiv:2105.11038.

[49] P. Kumar, S. Sendelbach, M. A. Beck, J. W. Freeland, Z. Wang, H. Wang, C. C. Yu, R. Q. Wu, D. P. Pappas, and R. McDermott, Origin and Reduction of $1/f$ Magnetic Flux Noise in Superconducting Devices, Phys. Rev. Appl. **6**, 041001(R) (2016).

[50] G. Catelani, X. S. Wu, and P. W. Adams, Fermi-liquid effects in the gapless state of marginally thin superconducting films, Phys. Rev. B **78**, 104515 (2008).

[51] M. Tinkham, *Introduction to Superconductivity* (Dover Publications, Mineola, NY, USA, 2004), 2nd ed.

[52] D. Bothner, T. Gaber, M. Kemmler, D. Koelle, R. Kleiner, S. Wünsch, and M. Siegel, Magnetic hysteresis effects in superconducting coplanar microwave resonators, Phys. Rev. B **86**, 014517 (2012).

[53] C. Song, T. W. Heitmann, M. P. DeFeo, K. Yu, R. McDermott, M. Neeley, J. M. Martinis, and B. L. T. Plourde, Microwave response of vortices in superconducting thin films of re and al, Phys. Rev. B **79**, 174512 (2009).

[54] G. Stan, S. B. Field, and J. M. Martinis, Critical Field for Complete Vortex Expulsion from Narrow Superconducting Strips, Phys. Rev. Lett. **92**, 097003 (2004).

[55] N. Pompeo and E. Silva, Reliable determination of vortex parameters from measurements of the microwave complex resistivity, Phys. Rev. B **78**, 094503 (2008).

[56] B. Chiaro, *et al.*, Dielectric surface loss in superconducting resonators with flux-trapping holes, Supercond. Sci. Technol. **29**, 104006 (2016).

[57] J. Bylander, S. Gustavsson, F. Yan, F. Yoshihara, K. Harrabi, G. Fitch, D. G. Cory, Y. Nakamura, J.-S. Tsai, and W. D. Oliver, Noise spectroscopy through dynamical decoupling with a superconducting flux qubit, Nat. Phys. **7**, 565 (2011).

[58] C. Wang, C. Axline, Y. Y. Gao, T. Brecht, Y. Chu, L. Frunzio, M. Devoret, and R. J. Schoelkopf, Surface participation and dielectric loss in superconducting qubits, Appl. Phys. Lett. **107**, 162601 (2015).

[59] J. Bardeen, L. N. Cooper, and J. R. Schrieffer, Theory of superconductivity, Phys. Rev. **108**, 1175 (1957).

[60] G. Catelani, R. J. Schoelkopf, M. H. Devoret, and L. I. Glazman, Relaxation and frequency shifts induced by quasiparticles in superconducting qubits, Phys. Rev. B **84**, 064517 (2011).

[61] A. A. Clerk and D. W. Utami, Using a qubit to measure photon-number statistics of a driven thermal oscillator, Phys. Rev. A **75**, 042302 (2007).

[62] J. G. Kroll, *Magnetic field compatible hybrid circuit quantum electrodynamics*, Ph.D. thesis, school Delft University of Technology (2019).

[63] S. Krinner, S. Storz, P. Kurpiers, P. Magnard, J. Heinsoo, R. Keller, J. Luetolf, C. Eichler, and A. Wallraff, Engineering cryogenic setups for 100-qubit scale superconducting circuit systems, EPJ Quantum Technol. **6**, 2 (2019).

[64] B. Al'Tshuler, A. Aronov, and B. Spivak, The aaronov-bohm effect in disordered conductors, ZhETF Pisma Redaktsiiu **33**, 101 (1981).

[65] M. Gijs, C. Van Haesendonck, and Y. Bruynseraede, Quantum oscillations in the superconducting fluctuation regime of cylindrical a1 films, Phys. Rev. B **30**, 2964 (1984).

[66] V. Chandrasekhar, M. J. Rooks, S. Wind, and D. E. Prober, Observation of Aharonov-Bohm Electron Interference Effects with Periods h/e and $h/2e$ in Individual Micron-Size, Normal-Metal Rings, Phys. Rev. Lett. **55**, 1610 (1985).

[67] F. Pierre, A. B. Gougam, A. Anthore, H. Pothier, D. Esteve, and N. O. Birge, Dephasing of electrons in mesoscopic metal wires, Phys. Rev. B **68**, 085413 (2003).

[68] E. Shimshoni, P. M. Goldbart, and N. Goldenfeld, Josephson interference phenomena above t_c, Phys. Rev. B **48**, 9865 (1993).